

**Clustering of the Diffuse Infrared Light from the COBE DIRBE
maps. III. Power spectrum analysis and excess isotropic
component of fluctuations.**

A. Kashlinsky^{1,3}, J. C. Mather², S. Odenwald⁴

¹NORDITA, Blegdamsvej 17, DK-2100 Copenhagen, Denmark

²Code 685, NASA Goddard Space Flight Center, Greenbelt, MD 20771

³Raytheon STX, Code 685,

NASA Goddard Space Flight Center, Greenbelt, MD 20771

⁴Raytheon STX, Code 630,

NASA Goddard Space Flight Center, Greenbelt, MD 20771

Received _____; accepted _____

ABSTRACT

The cosmic infrared background (CIB) radiation is the cosmic repository for energy release throughout the history of the universe. The spatial fluctuations of the CIB resulting from galaxy clustering are expected to be at least a few percent on scales of a degree, depending on the luminosity and clustering history of the early universe. Using the all-sky data from the COBE DIRBE instrument at wavelengths 1.25 - 100 μm we attempt to measure the CIB fluctuations. In the near-IR, foreground emission is dominated by small scale structure due to stars in the Galaxy. There we find a strong correlation between the amplitude of the fluctuations and Galactic latitude after removing bright foreground stars. Using data outside the Galactic plane ($|b| > 20^\circ$) and away from the center ($90^\circ < l < 270^\circ$) we extrapolate the amplitude of the fluctuations to $\text{cosec}|b| = 0$. We find a positive intercept of $\delta F_{\text{rms}} = 15.5^{+3.7}_{-7.0}, 5.9^{+1.6}_{-3.7}, 2.4^{+0.5}_{-0.9}, 2.0^{+0.25}_{-0.5}$ $\text{nWm}^{-2}\text{sr}^{-1}$ at 1.25, 2.2, 3.5 and 4.9 μm respectively, where the errors are the range of 92% confidence limits. For color subtracted maps between band 1 and 2 we find the isotropic part of the fluctuations at $7.6^{+1.2}_{-2.4}$ $\text{nWm}^{-2}\text{sr}^{-1}$. Based on detailed numerical and analytic models, this residual is not likely to originate from the Galaxy, our clipping algorithm, or instrumental noise. We demonstrate that the residuals from the fit used in the extrapolation are distributed isotropically and suggest that this extra variance may result from structure in the CIB. We also obtain a positive intercept from a linear combination of maps at 1.25 and 2.2 μm . For $2^\circ < \theta < 15^\circ$, a power-spectrum analysis yields firm upper limits of $(\theta/5^\circ) \times \delta F_{\text{rms}}(\theta) < 6, 2.5, 0.8, 0.5$ $\text{nWm}^{-2}\text{sr}^{-1}$ at 1.25, 2.2, 3.5 and 4.9 μm respectively. From 10 - 100 μm , the dominant foregrounds are emission by dust in the Solar system and the Galaxy. There the upper limits on the CIB fluctuations are below 1 $\text{nWm}^{-2}\text{sr}^{-1}$ and are lowest (≤ 0.5 $\text{nWm}^{-2}\text{sr}^{-1}$) at 25 μm .

Subject headings: Cosmology - Cosmic Background Radiation - Galaxies: Clustering - Galaxies: Evolution

1. Introduction

Diffuse backgrounds and their structure contain important information about the history of the early Universe, when discrete objects either do not exist or are not accessible to telescopic studies. The formation and early evolution of galaxies should have generated radiation redshifted into the infrared bands (e.g. Partridge and Peebles 1967; Bond et al. 1986). This cosmic infrared background (CIB) may come from the entire history of the Universe between the epoch of last scattering, mapped by the microwave background, and the present day.

The COBE Diffuse InfraRed Background Experiment (DIRBE) (Boggess et al. 1992; Silverberg et al. 1993; Weiland et al., DIRBE Explanatory Supplement, 1998) mapped the entire sky with 0.3° pixels and 0.7° resolution in ten bands between 1.25 and 240 μm . The results have been published (Hauser et al. 1998; Kelsall et al. 1998; Arendt et al. 1998; Dwek et al., 1998), based on a zodiacal light model believed accurate within a few percent (Kelsall et al. 1998). Their Galactic dust emission model (Arendt et al. 1998) is derived from fits to the DIRBE data and comparison to hydrogen maps, and accounts for the variation of dust temperature. Their model for Galactic starlight is derived from external star count models, with no free parameters. The residuals from the modeling were not significantly above the uncertainties except at 140 and 240 μm . The FIRAS instrument on COBE gave similar answers, (Fixsen, Mather, Bennett, and Shafer, 1998), using three different methods for removing the foregrounds. The agreement is significant because the instruments were calibrated independently. The measured values of the far-IR background are comparable to the total observed Galactic emission at visible and near-IR wavelengths, and imply that about half of the luminosity of the universe has been obscured by dust and converted into far-IR radiation. Some distant galaxies might be more reddened or obscured by dust than otherwise expected, and the CIB and its fluctuations might be brighter than predicted from visible band galaxy counts.

In this paper we continue our search for a CIB by trying to detect its spatial structure in the DIRBE data. The method is similar to that first suggested by Gunn and later applied in the visible (Shectman 1973, 1974) and UV (Martin and Bowyer 1989). Recently, Vogeley (1998)

applied the method to the Hubble Deep Field constraining the amount of the visible cosmic background, concluding that there is very little visible cosmic background from unresolved sources. They considered arcsecond scales where fluctuations are dominated by random parts of individual galaxy (Vogeley 1998) or cluster (Shectman 1974) profiles. We apply the method to degree scales where the dominant contribution comes from galaxy clustering. Our previous results are described by Kashlinsky, Mather, Odenwald and Hauser (1996a; Paper I) and Kashlinsky, Mather and Odenwald (1996b; Paper II).

If we assume that the galaxies producing the CIB are clustered, the amplitude of the resulting CIB 2-point correlation function, $C(\theta)$, depends on the rate of the flux emission, dF/dz , and on the galaxy 2-point correlation function, $\xi(r; z)$. If the latter is known on the linear scales subtended by a given angle, measurements or upper limits on $C(\theta)$ can constrain the levels of the CIB emitted by clustered material. Measuring or limiting the structure of the CIB can be especially valuable in the mid- to far-IR bands where the foreground emission is very bright, but smooth.

The plan of the paper is as follows: In Sec. 2 we define the quantities used and provide mathematical background. We show that for the measured galaxy correlation function we expect fluctuations of about 5 to 10% in the CIB flux on 0.5° scales, almost independently of the particular mechanism of the CIB production. We discuss our search for the CIB structure in the DIRBE data between 1 and $100 \mu\text{m}$. The last two bands of DIRBE - 140 and $240 \mu\text{m}$ - are not useful for this because of the large instrument noise there. Section 3 deals with the beam profile and the spatial window function for power spectrum analysis. Section 4 discusses the data for $\lambda \leq 5 \mu\text{m}$, where the foregrounds are dominated by stellar emission from the Galaxy. We find a significant trend in the amplitude of the measured fluctuations with Galactic latitude. When our star removal algorithm is applied to simulated data, we recover the measured slope of the correlation with Galactic latitude, and extrapolation of the simulated fluctuations to $\text{cosec}|b| = 0$ leads to a zero intercept. We derive a formula relating the measured fluctuations to star counts and show that for a plane-parallel Galaxy there should be a simple relationship between the b

dependence of the fluctuations and the slope of the star counts function at the Galactic pole. Then we show that for $90^\circ < l < 270^\circ$ and $|b| > 20^\circ$ the measured structure of the Galaxy fits the plane-parallel model. Furthermore, the scatter in the $C(0)$ - $\text{cosec}|b|$ plot is low enough to allow an extrapolation to $\text{cosec}|b| = 0$, with positive intercepts in all four near-IR bands. We perform a power spectrum analysis but most of the measured structure is due to fluctuating star counts. If the star removal algorithm removes stars fainter than 5 times the confusion noise limit, there are too few pixels left to calculate a power spectrum. Nevertheless, limits are sufficiently low to be of interest in testing theoretical predictions. We test our methods with numerical and analytic models of the Galaxy and possible CIB contributions and find good agreement with the data. Results from the mid- to far-IR bands, where foreground emission structure is dominated by the large scale gradients from dust emission in the Solar System and the Galaxy, are presented in Sec. 5. The upper limits on these fluctuations are $< 1 \text{ nWm}^{-2}\text{sr}^{-1}$, depending on wavelength, and provide much stronger tests of the predictions of galaxy counts than do direct measurements from inside the zodiacal dust cloud. We summarize our results in Sec. 6.

2. Theoretical preliminaries

Here we provide a general mathematical basis without specific cosmological and galaxy evolution models. We will use the data to constrain the CIB properties in a model-independent way, and then to constrain models of galaxy evolution. We extend our previous work (Paper I,I; Jimenez & Kashlinsky 1999) to show the power spectrum of the fluctuations and to estimate the typical amplitude of the fluctuations in a model-independent way.

We start with definitions. The surface brightness in the CIB per unit wavelength will be denoted as I_λ , per unit frequency as I_ν , and per logarithmic wavelength interval $F = \lambda I_\lambda = \nu I_\nu$, and we call them all “flux.” The fluctuation in the CIB flux is then $\delta F(\mathbf{x}) = F(\mathbf{x}) - \langle F \rangle$, where \mathbf{x} is the two dimensional coordinate on the sky and $\langle \dots \rangle$ denotes ensemble averaging. We also use the two-dimensional Fourier transform, $\delta F(\boldsymbol{\theta}) = (2\pi)^{-2} \int \delta F_{\mathbf{q}} \exp(-i\mathbf{q} \cdot \boldsymbol{\theta}) d^2\mathbf{q}$.

If $\delta F(\mathbf{x})$ field is a random variable, then it can be described by the moments of its probability distribution function. The first non-trivial moment is the projected 2-dimensional correlation function $C(\theta) = \langle \delta F(\mathbf{x} + \theta) \delta F(\mathbf{x}) \rangle$. The 2-dimensional power spectrum is $P_2(q) \equiv \langle |\delta F_q|^2 \rangle$, where the average is performed over all phases. The correlation function and the power spectrum are a pair of 2-dimensional Fourier transforms and for isotropically distributed signal are related by

$$C(\theta) = \frac{1}{2\pi} \int_0^\infty P_2(q) J_0(q\theta) q dq, \quad (1)$$

$$P_2(q) = 2\pi \int_0^\infty C(\theta) J_0(q\theta) \theta d\theta, \quad (2)$$

where $J_n(x)$ is the n -th order cylindrical Bessel function. If the phases are random, then the distribution of the flux field is Gaussian and the correlation function, or its Fourier transform the power spectrum, uniquely describe its statistics. In measurements with a finite beam radius ϑ the intrinsic power spectrum is multiplied by the window function W of the instrument. Another useful quantity is the mean square fluctuation within a finite beam, or zero-lag correlation signal, which is related to the power spectrum by

$$\begin{aligned} \langle (\delta F)^2 \rangle_\vartheta &= \frac{1}{2\pi} \int_0^\infty P_2(q) W_{TH}(q\vartheta) q dq \\ &\sim \frac{1}{2\pi} q^2 P_2(q)|_{q \sim \pi/2\vartheta}. \end{aligned} \quad (3)$$

For a top-hat beam the window function is $W_{TH} = [2J_1(x)/x]^2 = 0.5$ at $x \simeq \pi/2$ where $x = q\vartheta$, and hence the values of q^{-1} correspond to fluctuations on angular scales of diameter $\sim \pi/q$.

The CIB flux and its structure are measured in projection on the celestial sphere and reflect both the 3-dimensional clustering pattern of the galaxy distribution and the rate of emission at redshift z . We introduce the 3-dimensional two-point correlation function of galaxy clustering, $\xi(r)$, and its 3-dimensional power spectrum, $P_3(k)$. These are related via 3-dimensional Fourier transforms, and assuming isotropy are related by

$$\xi(r) = \frac{1}{2\pi^2} \int_0^\infty P_3(k) j_0(kr) k^2 dk. \quad (4)$$

The projected CIB correlation function is related to the underlying two-point correlation

function of the galaxy distribution and the rate of the CIB flux emission via the Limber equation

$$C(\theta) = \int_{z_1} \int_{z_2} \frac{dF}{dz_1} \frac{dF}{dz_2} \xi(r_{12}; z) dz_1 dz_2, \quad (5)$$

where r_{12} is the proper length subtended by the angle θ and redshifts z_1, z_2 . In the limit of small angles, $\theta \ll 1$, the Limber equation becomes (e.g. Peebles 1980)

$$C(\theta) = \int_0^\infty dz \left(\frac{dF}{dz} \right)^2 \int_{-\infty}^\infty \xi(r_{12}; z) du. \quad (6)$$

For Robertson-Walker metrics the proper separation is given by

$$r_{12}^2 = \left(\frac{dx/dz}{\sqrt{1-kx^2}} u \right)^2 + \frac{x^2(z)\theta^2}{(1+z)^2} \quad (7)$$

$$= c^2 \left(\frac{dt}{dz} \right)^2 u^2 + d_A^2(z)\theta^2. \quad (8)$$

Here $d_A(z)$ is the angular diameter distance, $x(z) \equiv d_A(z)/(1+z)$, u is the integration variable and t is the cosmic time.

The comoving volume occupied by a unit solid angle in the redshift interval dz is $dV/dz = (1+z)x^2(z)cdt/dz$, and the power received per unit wavelength and collecting area in band λ from each galaxy with absolute bolometric luminosity L at redshift z is $[L/(4\pi x^2(1+z)^3)]f_\lambda(\frac{\lambda}{1+z}; z)$. Here $f_\lambda d\lambda$ is the fraction of the total light emitted in the wavelength interval $[\lambda; \lambda + d\lambda]$ and the extra factor of $(1+z)$ in the denominator accounts for the fact that the flux received in band λ comes from a redshifted galaxy. The contribution to the total CIB flux from the redshift interval dz is given by

$$\frac{dF}{dz} = \frac{R_H}{4\pi} \frac{1}{(1+z)^2} \frac{d(H_0 t)}{dz} \sum_i \mathcal{L}_i(z) [\lambda f_{\lambda,i}(\frac{\lambda}{1+z}; z)], \quad (9)$$

where the sum is taken over all galaxy populations contributing flux in the observer rest-frame band at λ , and f_λ characterizes the spectral energy distribution (SED) of galaxy population i . Here $R_H = cH_0^{-1}$ and $\mathcal{L}(z) = \int \Phi(L; z)LdL$ is the comoving luminosity density from galaxies with the luminosity function $\Phi(L; z)$ at epoch z .

It is illustrative to study the redshift dependence of the flux rate production, Eq. (9). At small redshifts the factor $(1+z)^{-2}dt/dz$ varies little with z , and the rate of flux production is

governed by the comoving bolometric luminosity density $\mathcal{L}(z)$ and the SED of the galaxy emission f_λ . If the luminosity evolution at these redshifts is small, the rate of flux production is governed by the SED shape. If $f_\lambda(\lambda)$ increases towards shorter wavelengths then dF/dz increases with z . For $\lambda f_\lambda = \text{const}$, and no luminosity evolution, the rate is roughly constant with small z . In addition, there is observational evidence for an increase of $\mathcal{L}(z)$ out to $z \simeq 1$ in the galaxy rest-frame UV to near-IR ($1 \mu\text{m}$) bands (Lilly et al. 1996). At sufficiently high redshifts, the evolution in Eq. (9) would be offset by the factor $(1+z)^{-2} dt/dz$, so that the rate of production would be cut off at sufficiently large z . This factor is responsible for resolving Olbers' paradox even for a flat SED.

The SED for rest-frame $\lambda < 10\mu\text{m}$ is dominated by stellar emission, with a peak at visible wavelengths and a decrease for $\lambda > 0.7 \mu\text{m}$. Consequently, most of the predicted J band CIB comes from redshifts $z \sim 0.3 - 1$, which shifts the visible emission of normal stellar populations into the J band; cf. Yoshii and Takahara (1988). In the M band at $5 \mu\text{m}$, most of the predicted CIB comes from $z > 1 - 2$. At $\lambda > 10 \mu\text{m}$, the emission is dominated by galactic dust and the situation is reversed, so f_λ increases with wavelength roughly as λ^α with $\alpha \sim 1.5$. Hence, the dusty star-burst galaxies observed by IRAS at low redshifts should make the dominant contribution to the $10 \mu\text{m}$ CIB. In the far-IR, the measured CIB found by DIRBE can have large contributions from high redshifts.

Measurements of the correlation function $C(\theta) = \langle \delta F(\mathbf{x} + \theta) \delta F(\mathbf{x}) \rangle$ have an important advantage over direct determinations of the CIB spatial power spectrum, because they are immune to the discontinuities in the maps created by point source removal. (Because, in practice, $C(\theta)$ is evaluated from masked data, the uncertainties of the $C(\theta)$ points are themselves correlated.) However, interpreting $C(\theta)$ in terms of dF/dz and $\xi(r)$ can be cumbersome because the right-hand-side of (6) contains a double integral and the 3-dimensional correlation function is not always positive. By definition, $\xi(r)$ must be negative on large scales so that $\int_0^\infty \xi(r) r^2 dr = 0$.

A simpler method is to work with the Fourier transform of the correlation function, $P_2(q)$, which contains the same information as $C(\theta)$ and is easier to interpret. As for $C(\theta)$ the effects of the mask will produce correlations of the power spectrum points with each other. Also, the

measured power spectrum is the convolution of the Fourier transform of the mask with the true power. Although the uncertainties in $C(\theta)$ and $P_2(q)$ can be evaluated from theory, we evaluated them from the data by comparing multiple measurements.

The Limber equation (6) can be rewritten directly in terms of the power spectra, substituting Eq. (4) into (6) and using $\int_{-\infty}^{\infty} j_0(\sqrt{x^2 + y^2})dy = \pi J_0(x)$ to obtain

$$C(\theta) = \frac{1}{2\pi} \int_0^{\infty} dz \left(\frac{dF}{dz} \right)^2 \frac{1}{cdt/dz} \int_0^{\infty} P_3(k; z) J_0(kd_A\theta) k dk. \quad (10)$$

Substituting this expression into (2) and using the orthogonality relations for the Bessel functions, $\int_0^{\infty} J_0(\alpha\theta)J_0(\beta\theta)\theta d\theta = \alpha^{-1}\delta_D(\alpha - \beta)$, leads to

$$P_2(q) = \int_0^{\infty} \left(\frac{dF}{dz} \right)^2 \frac{(1+z)^2}{c \frac{dt}{dz} x^2(z)} P_3(qd_A^{-1}(z); z) dz. \quad (11)$$

Equation(11) involves only one integration and the kernel is always positive. Hence it may be easier to derive cosmologically interesting quantities such as F and $\xi(r)$ or $P_3(k)$. Determining $P_2(q)$ directly from the data is difficult owing to the masking created by point source removal, and it seems best to compute $C(\theta)$ and then derive $P_2(q)$ from it.

Figure 1a plots the argument, $q(1+z)/x(z)$, of P_3 in the right-hand-side of Eq. (11) for the largest wavenumbers (smallest scales) probed by DIRBE at various redshifts z . The dotted line corresponds to $\Omega = 1, \Omega_\Lambda = 0$; the solid to $\Omega = 0.1, \Omega_\Lambda = 0$ and the dashes to $\Omega = 0.1, \Omega_\Lambda = 0.9$, where $\Omega_\Lambda = 3H_0^2(1 - \Omega)$ denotes the contribution of the cosmological constant. For redshifts contributing most of the CIB flux ($z > 0.1-0.2$, cf. Paper I), the DIRBE instrument probes scales which are in the quasi-linear or linear regime, and which thus can be approximated as having evolved at the same rate with time. Thus for DIRBE scales, one can write $P_3(k; z) \simeq P_3(k; 0)\Psi^2(z)$, (e.g. Peebles 1980), where $\Psi^2(z)$ accounts for the evolution of the clustering and is normalized to $\Psi^2(0) = 1$. Then Eq. (11) can be rewritten in a more compact way:

$$q^2 P_2(q) = \int_0^{\infty} \left(\frac{dF}{dz} \right)^2 \frac{\Psi^2(z)}{H_0 \frac{dt}{dz}} \Delta^2 \left(\frac{q}{d_A(z)} \right) dz, \quad (12)$$

with

$$H_0 \frac{dt}{dz} = \frac{1}{(1+z)^2 \sqrt{1 + \Omega z + \Omega_\Lambda [(1+z)^{-2} - 1]}}. \quad (13)$$

The left-hand-side of (12) is the same order of magnitude as the mean square fluctuation (3), and we have defined

$$\Delta^2(k) \equiv R_H^{-1} k^2 P_3(k; 0). \quad (14)$$

The quantity $\Delta(k)$ is roughly the fluctuation over the line-of-sight cylinder of length R_H and diameter k^{-1} . For relevant scales and spectra of density fluctuations, $\Delta(k)$ increases with k . Hence, the CIB fluctuation on a scale of k^{-1} is $\sim \sqrt{k^2 P_2(k)} \sim F \Delta(k/R_H)$.

The present day power spectrum of galaxy clustering has been measured on scales corresponding to at least the smallest angular scales probed by DIRBE. The most accurate measurement comes from the APM survey data on the projected angular correlation function (Maddox et al. 1990). Baugh and Efstathiou (1993) deprojected the APM data to obtain the underlying power spectrum of galaxy clustering, $P_3(k)$. Kashlinsky (1998) used the current large scale data, and the abundance of objects at high redshifts, to reconstruct the pregalactic density field over six orders of magnitude in mass. His result requires significant fluctuation power on small scales, an early epoch of galaxy formation, and high levels of the CIB and its fluctuations. Fig. 1b plots the data from the Baugh and Efstathiou (1993) deprojection. On small scales (large k), $\Delta^2(k) \propto k^{0.7}$, so the integrand in Eq. (12) behaves as $\propto z^{-0.7}$ with an integrable singularity at $z \rightarrow 0$. While a non-negligible part of the clustering part of the CIB fluctuations comes from nearby galaxies, much of it arises from galaxies at $z > 1$.

In Papers I and II we estimated $\sim 5\text{-}10\%$ CIB fluctuations on a scale of 0.5° . One can also see this in a more intuitive way from Eq. (12). Fig. 1a plots $q(1+z)/x(z)$, the largest wavenumber that enters on the right hand side of (12), for $q^{-1} = 0.5^\circ$. In the Friedman-Robertson-Walker Universe, $q/d_A(z)$ reaches a minimum at $z \sim 1 - 3$, and its value at the minimum depends weakly on cosmological parameters. Thus (12) can be rewritten as an inequality:

$$q^2 P_2(q) \geq \Delta^2 \left(\min \left[\frac{q}{d_A(z)} \right] \right) \int_0^\infty \left(\frac{dF}{dz} \right)^2 \frac{\Psi^2(z)}{H_0 \frac{dt}{dz}} dz. \quad (15)$$

On linear and quasi-linear scales over the range of redshifts that contribute most to the CIB, the quantity $\Psi^2(z)/\frac{H_0 dt}{dz}$ depends weakly on z (e.g. on linear scales $\Psi^2 = (1+z)^{-2}$ if $\Omega = 1$). The integral is of the same order of magnitude as F^2 because the term dF/dz is a peaked function with a full width at half maximum of order unity. Hence, the relative fluctuation in the CIB is $\sim \Delta(\min[\frac{q}{d_A(z)}])$. Fig. 1b plots $\Delta(k)$ vs. k using the power spectrum of APM galaxies from Baugh & Efstathiou (1993); it is an increasing function of k . At the wavenumber of the minimum in Fig. 1a, the CIB fluctuation can be as large as $\sim (5-10)\%$. In models where the bulk of the CIB comes from higher redshifts, this number may be somewhat smaller. Because this method measures a two-point process, the results constrain a measure related to the mean square of the CIB emission rate, i.e. $\sim \int \left(\frac{dF}{dz}\right)^2 dz$.

Many models have calculated the expected CIB over the 1 - 100 μm range (e.g. Partridge and Peebles 1967; Stecker et al. 1977; Bond et al. 1986; Fall et al. 1996; Wang 1991; Beichman and Helou 1991; Franceschini et al. 1991; Cole et al. 1992; Malkan and Stecker, 1997; Jimenez and Kashlinsky 1999; Dwek et al. 1998). The models are normalized to galaxy counts and predict a typical flux of $F \sim 10 \text{ nWm}^{-2}\text{sr}^{-1}$. Deep K band counts of galaxies (e.g. Cowie et al. 1994; Djorgovski et al. 1995) or at 12 - 100 μm (Hacking and Soifer 1991) suggest minimal fluxes of at least a few $\text{nWm}^{-2}\text{sr}^{-1}$. Therefore the CIB fluctuations on 0.5° scales may be $\sim 1 \text{ nWm}^{-2}\text{sr}^{-1}$.

The APM measurements of the galaxy correlation function in the blue band might not apply to the infrared. However, the r band Palomar survey (Picard 1991), and the R-band Las Campanas survey (Schechter et al. 1996, Lin et al. 1996) give results identical to the APM survey. On the other hand, for IRAS galaxies on small (non-linear) scales the correlation function has a lower coherence length. Saunders et al. (1992) show that on small scales IRAS galaxies at $60\mu\text{m}$ cluster with $\xi_{IRAS} = (r/r_{*,IRAS})^{-1-\gamma_{IRAS}}$ where $r_{*,IRAS} \simeq 4h^{-1}\text{Mpc}$ and $\gamma_{IRAS} \simeq 0.6$, as opposed to $r_* = 5.5h^{-1}\text{Mpc}$ and $\gamma \simeq 0.7$ for the APM galaxies (Moore et al. 1994). The slight difference could be due a tendency of the IRAS dusty star-burst galaxies to avoid the central regions of rich clusters of galaxies. However, on larger (linear) scales where the galaxy clustering pattern presumably traces the pregalactic density field, IRAS galaxies as measured by

the QDOT counts-in-cells analysis (Saunders et al. 1990) are consistent with the APM galaxies power spectrum. These linear to quasi-linear scales are relevant for the DIRBE beam size, so we use the APM numbers for all infrared wavelengths. In surveys with smaller beams, the differences will be more pronounced, but the differences between the IRAS and APM correlation functions do not lead to appreciably smaller mid- to far-IR CIB fluctuations.

In addition to the clustering term, there is a white-noise component in the correlation signal due to individual galaxies (e.g. Peebles 1980). Its amplitude at zero lag is

$$C_{\text{WN}}(0) = \theta_{\text{beam}}^{-2} \frac{R_H}{16\pi^2} \int \frac{\Phi(L; z) L^2 dL}{x^2(z)(1+z)^8} \frac{H_0 dt}{dz} \left[\lambda f_\lambda \left(\frac{\lambda}{1+z}; z \right) \right]^2 dz. \quad (16)$$

Like white noise from discrete stars, the white noise from galaxies is dominated by the nearest objects, unlike the clustered component (6), because of the presence of $x^2(z)$ in the denominator of the integrand in (16). Because the galaxies are almost undetectable against the star fluctuations, the galaxy white noise is also negligible.

3. DIRBE data and beam profile

The COBE DIRBE instrument provided an all-sky 41 week survey with a ten-band photometer (Boggess et al. 1992). The DIRBE bolometer measurements at 140 and 240 μm are too noisy for our purposes. The remaining eight bands are centered on wavelengths 1.25, 2.2, 3.5, 4.9, 12, 25, 60 and 100 μm , and are labeled Bands 1-8 respectively. We obtained the 41 weekly-averaged DIRBE maps from the National Space Science Data Center (NSSDC), subtracted the zodiacal light model developed by the DIRBE team (Kelsall et al. 1998; Weiland et al, 1998, DIRBE Explanatory Supplement), and averaged the weeks together.

The maps are stored in a cube format and pixelized into 6 faces of 256^2 approximately square pixels $\sim 0.3^\circ$ on a side. For a finite beam the ideal map is convolved with the beam window function. For a circular top-hat beam similar to DIRBE’s square top hat, the Fourier

transform of the window function is $W(x) = [2J_1(x)/x]^2$, where $J_1(x)$ is the first-order cylindrical Bessel function. The measured power spectrum is then the product of the underlying power spectrum and the beam window function, i.e. $P_{\text{measured}}(q) = P_2(q)W(q\vartheta)$ where ϑ reflects the beam size. On large scales (small q), $W(x) \sim 1$. Throughout the rest of the paper, $P(q)$ will refer to the 2-dimensional power spectrum of the diffuse emission computed from DIRBE maps after deconvolution from the beam profile, i.e. $P(q) = P_{\text{measured}}(q)/W(q\vartheta)$.

We determined the effective W and the effective beam size from maps of the beam response function archived at the NSSDC with 181×225 0.0065° square pixels, which we embedded in 256^2 , 512^2 , and 1024^2 pixel arrays. The results for Band 1 are shown in Fig. 2, and are similar for all eight bands. The solid line shows a top-hat beam profile with $\vartheta = 0.4^\circ$ which is slightly lower than the value of $\vartheta = 0.45^\circ$ adopted in Paper I. From eye fits we adopted $\vartheta = 0.4^\circ$ in Band 1, 0.37° in Bands 2 and 3, and 0.35° in Bands 4 to 8. The combined effects of beam smearing from the motion of the beam during sampling, pixelization, and pointing error would increase the effective beam size by about 10%, and agree better with Paper I. The beam response function drops below 10% at $q^{-1} < 0.15^\circ$ and the pixelization prevents measurement below $q^{-1} = 0.1^\circ$.

4. Near-IR analysis

4.1. Foregrounds and point source removal

Foreground emission from the Galaxy and the solar system is the main problem in unveiling the expected CIB. At wavelengths less than $10 \mu\text{m}$, the dominant foreground after removing the zodiacal light model is emission from stars in our Galaxy. Using the SAO Bright Star Catalog magnitudes and colors, we simulated J band maps. We found that aside from the large-scale shape of the galaxy and a few star clusters this foreground has an almost uncorrelated spatial distribution. At 12 and $25 \mu\text{m}$ (DIRBE Bands 5 and 6) the zodiacal dust is so bright that residuals from the model subtraction dominate the map structure outside the Galactic plane. At wavelengths of 60 and $100 \mu\text{m}$ (DIRBE bands 7 and 8) most foreground residual fluctuations come

from cirrus dust clouds in the Galaxy, and stars contribute little.

The measured fluctuations contributed by point sources can be reduced substantially by identifying and removing them down to near the confusion noise limit. We used the point source finding routine developed by the DIRBE team and adopted in Paper I, and call it the “clipping” algorithm. The data from a selected region (patch) are first used to construct a smoothed model of the sky background emission for the whole patch, as follows. Surrounding each pixel, a window of size $f_{\text{size}} \times f_{\text{size}}$ is searched for the minimal flux value. We use the minimal value rather than the median because the stellar brightness distribution is highly skewed. The map of this minimal (or lower envelope) flux is then fitted to a 2-dimensional polynomial surface of order n_{fit} . This polynomial is in turn subtracted from the sky map, and the standard deviation σ_0 is calculated. Then, each of the pixels with flux above $N_{\text{cut}}\sigma_0$ is masked out along with the 8 adjacent pixels, about twice the DIRBE beam area. This process of fitting a polynomial, identifying bright pixels, and masking them out, is iterated about 5 times, until no more fluxes above $N_{\text{cut}}\sigma_0$ are found. In the near-IR no noticeable improvement is reached above $n_{\text{fit}} = 2$. We discuss the dependence on f_{size} in Sec. 4.5; for the results presented below we used $f_{\text{size}} = 5$. The polynomial fit was used only for point source masking, no gradients were subtracted from the maps analyzed in this (near-IR) section, and the results at high galactic latitude ($|b| > 20^\circ$) were independent of this choice.

For the near-IR, where foreground stars are the dominant source of fluctuations, there should be a clear correlation between the fluxes at different wavelengths. Furthermore, because most of the flux and fluctuations come from K and M stars, and the DIRBE pixels are large enough to include many stars, the dispersion in the color diagrams for the four near-IR bands should be small. In Paper I we used these properties to search for CIB fluctuations that have a different color due to redshifts or a different source spectrum. We construct a linear combination of maps at two different bands:

$$\Delta_{12} = \delta F_1 - \beta_{12}\delta F_2. \tag{17}$$

Note that this Δ is unrelated to the Δ of Eq. (12). The variance of this map, $C_\Delta(0) \equiv \langle \Delta_{12}^2 \rangle$, is

minimized for

$$\beta_{12} = \frac{\langle \delta F_1 \delta F_2 \rangle}{\langle \delta F_2^2 \rangle}. \quad (18)$$

Because the dispersion in the color index $\beta = \delta F_1 / \delta F_2$ is small, i.e. $\sigma_\beta = \sqrt{\langle \beta^2 \rangle - \langle \beta \rangle^2} \ll \beta_{12}^2$ with the average taken over all the pixels in the patch, the foreground contribution to $C(0)$ will be reduced by a factor $\sim (\beta_{12} / \sigma_\beta)^2 \gg 1$. If the fluxes in adjacent bands do not correlate, the emission in the two bands comes from different sources or from measurement errors (noise).

Since most of the predicted CIB comes from galaxies at $z > 0.2$ with typical stellar populations, its color should differ from that of the foreground stars, and the color subtracted maps should retain some of the CIB structure. If most of the CIB comes from high redshifts so that

$$\beta_{CIB} = \langle \delta F_{1,CIB} \delta F_{2,CIB} \rangle / \langle \delta F_{2,CIB}^2 \rangle \leq 2\beta_{12}, \quad (19)$$

the CIB fluctuations in the color subtracted maps will be larger than in the single band maps. We used Eq. (18) to make all-sky color-subtracted maps for all the adjacent band pairs, in order to search for a coordinate-independent part of the fluctuations. This method can be generalized to a multi-color subtraction method, e.g. minimize $\Delta_{123} = \delta F_1 - \beta \delta F_2 - \alpha \delta F_3$ with respect to α, β . We applied this to the DIRBE maps, but without significantly different results.

4.2. All sky variance analysis: $C(0)$

We divided the sky into 384 patches, each with 32×32 pixels, and clipped each patch individually using the above procedure, with $N_{\text{cut}} = 7, 5, 3.5$ and 3 . Because the foreground emission at these wavelengths is dominated by point sources, very few pixels are left for $N_{\text{cut}} < 3$. We performed the same analysis on 96 patches of 64×64 pixels, with similar results.

Our star finding algorithm cuts deeper into the distribution than a simple interpretation might suggest. Each bright star is observed in about 5 pixels, depending on the position of the star. The noise distribution of these pixels in the absence of the bright star still has a non-Gaussian distribution with a non-zero mean. Therefore a star near the clipping threshold will be identified

in the pixel where the background noise fluctuations are greatest, rather than at the true star location. Hence, the clipping algorithm finds stars about 1σ fainter than N_{cut} , as we confirmed with simulations.

After clipping the 384 patches, we computed the color indices according to Eq. (18), the single band $C(0)$, and the color-subtracted $C_{\Delta}(0)$ for each patch. Figure 3 shows histograms of the numbers of the remaining pixels after clipping. In the near-IR bands, about 350-450 pixels out of 1024, or about uncorrelated 75-90 beams per patch, remain for $N_{\text{cut}} = 3.5, 3$, making the intrinsic uncertainty of $C(0)$ less than 15%.

In each patch there is a clear correlation between the fluxes in the adjacent bands. Paper I gave flux correlation plots for selected patches and an earlier model of the zodiacal light. The current data give similar results. For bands 1-4 all the patches have correlation coefficient $R > 0.9$ between all the pairs of bands. The color indices have very small dispersion, $\sigma_{\beta}/\beta < 10\%$. Because the dispersion in β is so small, and most of the predicted CIB emission at these wavelengths comes from redshifts $z > 0.1$, the CIB fluctuations should not be removed by the color subtraction.

Fig. 4 plots the histograms of β for $N_{\text{cut}} = 3$. The maps for the band pair [4, 5] have color index $\beta \simeq 0$ because the dust in the solar system is not strongly correlated with the stars seen in Band 4. Between Bands 1 and 2, most of the patches have a color index of $\beta_{12} \simeq 2$, typical of K-M giants. In band pairs [2, 3] and especially [3, 4] the spread in β is substantial, suggesting that star fluctuations are not the only source, or that their color is different in different regions. The range of color indices for the band differences [2 – 3] and [3 – 4] is reduced for $|b| > 20^\circ$, but nevertheless remains much wider than for the [1 – 2] maps. Most of the map peaks are due to stars, as we found them in simulated maps derived from the SAO Bright Star Catalog, using wavelength extrapolations appropriate to the tabulated spectral types.

The lowest limits on $C(0)$ for single bands are similar to those in Paper II, and for the color subtracted bands they are not very different from Paper I. However, we can now address the dependence of $C(0)$ on Galactic coordinates. Fig. 5 shows a strong correlation of $\sqrt{C(0)}$ with $\text{cosec}|b|$. Fig. 6 plots $\sqrt{C(0)}$ vs. $\text{cosec}|b|$ for the color subtracted maps [1-2], [2-3], and [3-4].

Although the color subtracted $C(0)$ is a factor of ~ 10 lower than for single bands, the residual fluctuations still depend strongly on Galactic latitude.

4.3. Near-IR fluctuations from Galactic stars

We would now like to extrapolate the data to estimate the extragalactic contribution to the fluctuations. We use analytic and numerical models to support a power-law dependence of the stellar contribution to $C(0)$ on $\text{cosec}|b|$. We also show how to extrapolate the fluctuations due to Galactic stars to $\text{cosec}|b| = 0$, and that we expect no isotropic residual for $C(0)$ due to stars.

We assume that Galactic stars are distributed with a white noise power spectrum, i.e. they are spatially uncorrelated except for large scale distribution functions such as those in the Bahcall and Soneira (1980) and Wainscoat et al. (1992) models. Thus $C(0)$ in the direction b is given by the following (Galactic) version of the Limber equation:

$$\begin{aligned}\sigma^2(x) &= \sum_i \int \frac{L_1}{4\pi r_1^2} \frac{L_2}{4\pi r_2^2} dP_{12} \\ &= \sum_i \frac{L_i^2}{4\pi} \omega \int_{R_i}^{\infty} \frac{n_i(r; x)}{r^2} dr.\end{aligned}\tag{20}$$

Here the sum is taken over stars of type i with intrinsic luminosity L_i , ω is the pixel solid angle, $x = \text{cosec}|b|$, r is the distance to each star, and n_i is the number density of stars at that distance in the direction of b . The distance to the star is related to the height, Z , above the Galactic plane by $r = Z \text{cosec}|b|$. In our clipping algorithm, we remove sources exceeding the flux limit of $N_{\text{cut}} \times (\text{standard deviation of the background polynomial fit})$. This standard deviation is approximately σ from Eq. (20) above, if the integration limits are chosen to match the threshold for star detection and clipping. We find a very good correlation between the deviation of the fit and the value of the residual fluctuations in the patch; if all the histograms had the same non-Gaussian shape the two should be proportional. Hence, the lower limit radius can be approximated to depend on σ itself via

$$R_i = [L_i / (4\pi N_{\text{cut}} \sigma)]^{1/2}.\tag{21}$$

Equations (20), (21) then allow us to determine $\sigma(b)$ for a given distribution of stars.

We now derive the latitude dependence implied by these equations. As an example, we use a plane parallel exponential model for stars in the Galaxy: $n_i = n_{0,i} \exp(-\frac{r}{h_i x})$. This should be valid if our clipping radius R is small compared to the exponential scale length for the Galactic disk $\alpha^{-1} \simeq (3 - 4)$ Kpc, and is in rough agreement with the disk in hydrostatic equilibrium with the Galactic gravity field (Mihalas & Binney 1981). Now Eq. (20) becomes

$$\sigma^2(x) = \sum_i R_i^{-1} \frac{L_i^2 n_{0,i} \omega}{4\pi} E_2\left(\frac{R_i}{h_i x}\right), \quad (22)$$

where $E_n(u) \equiv \int_1^\infty t^{-n} \exp(-ut) dt$. We express (22) in terms of the total number of stars in the dR_i interval:

$$\frac{dN_i}{dR_i} = n_{0,i} \omega R_i^2 \exp\left(-\frac{R_i}{h_i x}\right). \quad (23)$$

Then the equation for $\sigma(x)$ becomes:

$$1 = N_{\text{cut}}^2 \sum_i \left(R_i \frac{dN_i}{dR_i} \right) [\exp(q) E_2(q)]|_{q=R_i/h_i x}. \quad (24)$$

Consider first the limit when $R_i \ll h_i$. In this case $q < 1$ and the term in square brackets is near unity. The number of clipped stars per beam-width then becomes $N_{>} = \omega \sum_i \int_0^{R_i} n(r; x) r^2 dr \simeq 3^{-1} \sum_i (R_i dN_i/dR_i)$, leading to $N_{>} = N_{\text{cut}}^{-2}/3$. This is much smaller than we find in the data. Our clipping algorithm removes 9 pixels per star and cuts deeper than $N_{\text{cut}} = 3.5$ would indicate, and leaves only about 40% of the pixels. This proves that $q > 1$, i.e. bright stars are seen out to the scale height of the disk and beyond.

We now consider the variations in star counts with magnitude in a plane-parallel Galaxy. The differential counts in the magnitude interval dm are given by $dN/dm = \omega [d \ln r_m / dm] n(r_m) r_m^3$, where $r_m \propto 10^{0.2m}$ is the radial distance to the star of apparent magnitude m . In the limit of $r_m < h$, or $n \simeq \text{constant}$, the counts converge to the uniform distribution limit, $dN/dm \propto 10^{0.6m}$. In a plane-parallel Galaxy in which the radial structure can be neglected, the number density of stars depends only on $|Z| \propto 10^{0.2m} \sin |b|$, and the differential counts in the direction $x = \text{cosec} |b|$ can be related to those at the Galactic pole by

$$\frac{dN}{dm}|_x = x^3 \frac{dN(m - 5 \log_{10} x)}{dm}|_{\text{Pole}}. \quad (25)$$

Hence, once the counts at the pole are measured, we can evaluate the expected number counts in any direction b and then compute the fluctuations in the flux they produce via

$$\sigma^2(x) \propto \int_m^\infty 10^{-0.8m} \frac{dN}{dm} \Big|_x dm. \quad (26)$$

This formulation has two advantages: 1) the data on star counts in the polar regions can be used to evaluate the dependence of star fluctuations on $\text{cosec}|b|$; and 2) the only assumption is plane parallelism. We tested this assumption with both models and observations.

We now determine dN/dm from the DIRBE data, and compare with prior observations. Figure 7 shows a Band 2 histogram of $\log_{10}(|F - \langle F \rangle|)$ for a 128^2 pixel ($38.4^\circ \times 38.4^\circ$) region at the North Galactic Pole (NGP). This logarithmic form is useful for displaying both large and small deviations, and we have normalized it to the equivalent number of stars per magnitude per square degree. The equivalent K magnitude is plotted on the top horizontal axis. With the DIRBE beam of 1.42×10^{-4} sr (4.5 pixels), $F = 1 \text{ nWm}^{-2}\text{sr}^{-1}$ corresponds to $m_K = 9.45$. Because the CIB level and the smooth foreground contributions from dust and faint stars are not known in advance, we must subtract the mean of this confusion noise before seeking to measure brightnesses of individual bright stars. We define $\langle F \rangle$ as the mean flux of the map clipped with $N_{\text{cut}} = 3.5$; in this case it is $66 \text{ nWm}^{-2}\text{sr}^{-1}$ or $m_K = 5$, near the turnover of the distribution. The total number of pixels with positive values of the flux after the subtraction is 12,359; the remaining 24.6% of the pixels have negative fluxes. We have plotted both positive and negative deviations to illustrate the asymmetry of the histogram far from the peak, as well as its symmetry near the peak. Negative deviations are statistical fluctuations, while very bright pixels are individual cataloged stars. For the clipped map at $N_{\text{cut}} = 3.5$, a total of 6,380 pixels remain. Out of these, 2,982 pixels (47%) have positive fluxes, showing the symmetry of the flux distribution for the clipped map.

Figure 7 also shows a Gaussian distribution with the variance $\sigma \simeq 10 \text{ nWm}^{-2}\text{sr}^{-1}$ computed with $N_{\text{cut}} = 3.5$, and for $\sigma = 9 \text{ nWm}^{-2}\text{sr}^{-1}$. The difference between these two Gaussians is not large on this plot, showing the difficulty of direct detection of a sub-population of Gaussian fluctuations with dispersion of $5 \text{ nWm}^{-2}\text{sr}^{-1}$.

The NGP star counts were observed directly by Elias (1978). We show his data at $K = 1, 2.5, 3.25$ and 8 with $N^{1/2}$ error bars and our binning of his data. Further NGP data were obtained by the 2MASS survey in K_s band, almost identical to the DIRBE Band 2, and were kindly provided to us by Tom Jarrett (1998). The cumulative counts from these measurements were shown in Fig. 1 of Beichman (1996) out to $K_s > 15$, who found that they follow $dN/dm \propto 10^{0.3m}$ (cf. his Table 4). Actual 2MASS star counts from a region of 5 square degrees centered on the NGP are plotted in Fig. 7. The agreement between the DIRBE counts, the Elias (1978) and Jarrett (1998) data, and the $B = 0.3$ extrapolation is excellent over 15 magnitudes, or six decades in flux. South Galactic Pole counts from Minezaki et al. (1998) are also shown, and confirm the slope as well as the north-south symmetry of the Galaxy. At $m_K < 1.5$, the counts tend to the slope of $B = 0.6$ coming from stars much closer than the scale height; if B were less than 0.6, the integrated star brightness would diverge at the bright end.

The star counts agree with model predictions. Both Beichman (1996) in his Fig. 1 and Minezaki et al. (1998) in their Fig. 1 show that the counts are fitted well by extensions of either the Bahcall & Soneira (1980) or Wainscoat et al. (1992) models. An eyeball fit to their data gives $B = 0.3 - 0.32$ at $K = 11$. The Wainscoat et al. model at $K = 11$ shown in Fig. 1 of Minezaki et al. (1998) gives $\log dN/dm \simeq 1.35$, whereas continuation of the solid line in our Fig. 7 to $K = 11$ gives $\log dN/dm = 1.3$ if $B = 0.3$ and 1.4 if $B = 0.33$. The agreement between the two slopes and normalizations is thus very good. Even the large-beam DIRBE instrument sees far beyond the scale height of the bright K band stars.

We can now estimate the star brightness fluctuations. We begin with a power law for star counts in a plane-parallel Galaxy, $dN/dm|_{\text{Pole}} \propto 10^{Bm}$. Then the fluctuation due to stars fainter than m at the Galactic pole becomes:

$$\sigma^2|_{\text{Pole}} \propto \int_m^\infty 10^{-0.8m' + Bm'} dm'. \quad (27)$$

We now derive the latitude scaling law implied by these assumptions. In our clipping method the lower limit on m in the integral is given by $10^{-0.4m} \propto N_{\text{cut}}\sigma$. Combining this with Eq. (25) we

find that the fluctuation in the total star flux at latitude b is given by the power law

$$\sigma \propto (\operatorname{cosec}|b|)^{\frac{1.2}{B}-2}. \quad (28)$$

A uniform, infinite star cloud has $B = 0.6$, so there is no latitude dependence in that case. If $B = 0.4$, then we expect $\sigma \propto \operatorname{cosec}|b|$, while if $B = 0.3$ then $\sigma \propto \operatorname{cosec}^2|b|$. The dependence of $C(0)$ on $\operatorname{cosec}|b|$ can also be inverted via Eqs. (25), (26) to give a model for dN/dm . There is a unique relation between the two functions, for a plane-parallel Galaxy and our method of bright star extraction.

The value of N_{cut} enters indirectly, since it determines the magnitude m of the cutoff of detected stars and hence the magnitude at which B is important. Another measure of the star distribution function is the number of clipped stars, $N_{>}$. In the power law case we have a very simple result:

$$N_{>} = \frac{0.8 - B}{BN_{\text{cut}}^2} = \frac{2p + 1}{3N_{\text{cut}}^2}, \quad (29)$$

where $p = (1.2/B) - 2$ is the logarithmic slope in Eq. (28). The dependence of $N_{>} \propto N_{\text{cut}}^{-2}$ agrees with our results from DIRBE. Evaluating (29) for $B = 0.6$ (or $r_m < h$) we find $N_{>} = 1/3N_{\text{cut}}^2$, in agreement with the exponential distribution of Eq. (24) with $h = \infty$, while for $B = 0.3$ we find $N_{>} = 5/3N_{\text{cut}}^2$. The fraction of pixels clipped in the near-IR DIRBE maps at $N_{\text{cut}} = 3.5$ is $\sim 60\%$. Because the clipping algorithm uses a mask with about twice the beam area, this corresponds to $N_{>} = 0.35$ so the effective $N_{\text{cut}} = 2.2$ to 2.4 for $p = 2.0$ to 2.5 . The effective N_{cut} is less than the input value of 3.5 because each star is observed in many pixels, each with its own noise.

Similarly, Eqs. (25), (26) allow us to evaluate the expected variation of the residual fluctuation with N_{cut} , $\sigma \propto N_{\text{cut}}^{-1+0.8/B}$. In the limit of a spatially uniform distribution, $B = 0.6$, and $\sigma \propto N_{\text{cut}}^{1/3}$. For $B = 0.3$ it follows that $\sigma \propto N_{\text{cut}}^{1.7}$, and reducing N_{cut} from 7 to 3.5 should decrease $C(0)$ by a factor of 10 , in agreement with the DIRBE data.

To summarize this section, we have shown that, for $dN/dm \propto 10^{Bm}$ with $B = 0.3$ out to $K < 15$, and a plane-parallel Galaxy, we should recover a unique dependence for Galactic star fluctuations, $\sqrt{C(0)} \propto (\operatorname{cosec}|b|)^2$. This value of B is consistent with the N_{cut} dependence of the

fraction of clipped pixels and the amplitude σ of the remaining fluctuations in the DIRBE data.

4.4. Extrapolating to $\text{cosec}|b| = 0$

The scatter in Figs. 5 and 6 is large, because the plane-parallel model does not describe the large scale structure of the Galaxy. We divided the sample of 384 patches into four latitude bins and plot them against Galactic longitude l in Figs. 8 and 9. The dependence on longitude is significant for latitudes even as high as $|b| \sim 60^\circ$. However, for Galactic longitudes between 90° and 270° and high latitudes there is almost no longitude dependence. We therefore selected data with $90^\circ \leq l \leq 270^\circ$, and plot the dependence of $\sqrt{C(0)}$ on $\text{cosec}|b|$ in Figs. 10 and 11. The scatter is much reduced.

We tried several fitting functions for the 127 patches for which $|b| > 20^\circ$, $90^\circ < l < 270^\circ$:

$$\sqrt{C_{\text{fit}}(0)} = a + A(\text{cosec}|b|)^p, \quad (30)$$

where a presumably contains the cosmological and instrumental parts of the signal,

$$C_{\text{fit}}(0) = a^2 + A^2(\text{cosec}|b|)^{2p}, \quad (31)$$

$$\sqrt{C_{\text{fit}}(0)} = a + \sum_{i=1}^2 A_i(\text{cosec}|b|)^i, \quad (32)$$

and

$$C_{\text{fit}}(0) = a \exp(A \text{cosec}|b|), \quad (33)$$

minimizing, for example, $\langle [(C(0) - C_{\text{fit}})/C(0)]^2 \rangle$ with respect to a, A, p . The fits for Eq. (31) are shown in Figs. 10 and 11 and in Table 1. Except for the color-subtracted [2 – 3] maps, all fits give positive values of a . The color-subtracted maps [2 – 3] and [3 – 4] have large scatter in the color indices at which the variance $C_{\Delta}(0)$ is minimized, and do not allow for a robust determination of a . Note that $p > 1$ as expected from the model. The star and CIB fluctuations add in quadrature, as we demonstrated by simulation, so functional forms such as Eq. (31) are better justified than the other fits, although all give consistent results. The last row in Table 1 summarizes our limits

on a with errors corresponding to the extreme range from 92% confidence levels from all the fits, around our preferred central value from Eq. (31).

We estimated the statistical uncertainty as follows. We define a relative variance $\sigma_0^2 \equiv \min\langle[(\text{data} - \text{fit})/\text{data}]^2\rangle$ and a normalized $\chi_N^2(a, A, p) \equiv \langle[(\text{data} - \text{fit})/\text{data}]^2\rangle/\sigma_0^2$. Fig. 12 plots deviation histograms vs. $(\delta_{\text{fit}}/\sigma)^2$ where $\delta_{\text{fit}} \equiv (C(0) - a^2 - A^2x^{2p})/\sqrt{C(0)}$. For purely Gaussian deviations the histograms would be straight lines of slope $-1/2$.

We plot contours for $\Delta\chi^2 = 7$ which for 3 parameters (a, p, A) corresponds to a confidence level of 92%. Fig. 13 shows thus determined confidence contours projected onto the (a, p) plane for Bands 1 to 4, according to Eq. (31). The uncertainties shown in Table 1 correspond to the largest span of a in the panels in Fig. 12; for any given value of p the corresponding uncertainty levels are reduced significantly. This is the reason for the smaller formal uncertainties on a when an exponential fit - Eq. (33) - is assumed. Excluding from the analysis the patches that lie close to the Ecliptic plane further reduces the scatter in Figs. 10, 11, but the contours are almost identical to those in Fig. 13. Likewise, keeping only the patches at $120^\circ < l < 240^\circ$ produces the same result. The results for $N_{\text{cut}} = 7$ and 5 are consistent but with a larger uncertainty, whereas for $N_{\text{cut}} = 3$ the results are close to those shown in Table 1. The values for p are in good agreement with the expectations from the star counts. For Band 2, the maximal spread is $1.5 \leq p \leq 2.6$, which corresponds to $0.26 \leq B \leq 0.34$ in good agreement with Fig. 7.

To summarize, we have justified simple power law star count models and a plane parallel model of Galactic fluctuations by comparing the predictions to the measurements. The model applies only far from the Galactic center and Galactic plane. There is a statistically significant residual term in the DIRBE data after extrapolation to zero $\text{cosec}|b|$, with consistent values for four different fitting functions and for different N_{cut} . Plate 1 of our Paper II shows visually that there is no obvious structure in the selected anti-center $|b| > 20^\circ$ data set. We checked the validity of our simple models by studying the residuals of the fits. Fig. 14 shows the residuals for Eq. (31) for each patch fluctuations, $\sqrt{C(0)}$ in Band 2. There is no apparent correlation with Galactic longitude or latitude and the residuals are similarly independent of the ecliptic coordinates.

To consider whether the instrument itself or the zodiacal light could be a source for this residual, we review the estimates in Paper I. There we constructed maps of the differences between different weeks of observation, and found noise levels $\sqrt{C(0)} \sim 1.5, 0.3, 0.1 \text{ nWm}^{-2}\text{sr}^{-1}$ in Bands 1 through 3 for $N_{\text{cut}} = 3.5$. These are much smaller than a in Table 1, and it is unlikely that a is due to noise. Similar arguments apply to errors in the zodiacal light modeling, which varies from week to week, and would contribute to the measurement error calculation. In any case, in the near-IR bands the contribution of the zodiacal light is small. It should be largest at 12 and 25 μm , where the residual fluctuations are below $1 \text{ nWm}^{-2}\text{sr}^{-1}$ (Paper II and Sec. 5 of this paper), or $< 1\%$ of the total foreground. Therefore, the near-IR zodiacal modeling errors should be quite negligible compared to a . Furthermore, zodiacal light has a sharp cusp near the ecliptic plane, and zodiacal model errors would reflect this spatial dependence. We tried excluding patches in or near the ecliptic plane and found no change in a, p . The spatial correlation function that we find for $N_{\text{cut}} = 3.5$ (cf. Fig. 19) is significantly different from that expected for zodiacal light. The zodiacal light is smooth except near the ecliptic plane, where dust resonances and asteroid family debris are found.

We conclude that the single band plots all indicate a positive and approximately isotropic residual term that is unlikely to be produced by either instrumental noise or errors in the zodiacal modeling. Since independent contributions add linearly to the combined variance, such a component would contribute only $\sim 10\%$ to the total dispersion of the confusion noise at the faint end of the flux distribution plotted in Fig. 7, and would not be detectable there. The Figure shows two Gaussians differing in dispersion by 10%, and they both seem reasonable fits.

4.5. Analytic and Numerical Modeling

Since the measured residual a can not be explained by known errors, we must investigate the stellar foreground fluctuations more carefully. To do so, we simulated the confusion noise process both analytically and numerically.

Our analytical approach assumes a power law for dN/dm , with a Fourier method to simulate the histogram of Fig. 7. Let $\mathcal{P}(F)$ be the probability distribution function to find a single star in the line of sight with flux F . The probability distribution function and its characteristic function $G(f)$ are a pair of one dimensional Fourier transforms, $G(f) = \int \mathcal{P}(F) \exp(iff) dF$. The probability distribution function of finding two stars is the convolution of \mathcal{P} with itself and the characteristic function for it is $G^2(f)$. Similarly, for n stars the characteristic function is $G^n(f)$. For sufficiently large n the characteristic function tends to a Gaussian, which can be seen from expanding $G(f) \simeq 1 - f^2 \langle F^2 \rangle$, (Chandrasekhar 1954). For a Poisson distribution with m stars per pixel on the average, the probability to find n stars in a given pixel is $\mathcal{P}(n) = m^n \exp(-m)/n!$. Then the complex Fourier transform of the Poisson distribution of stars with an average of m stars per pixel is $\exp(m(G - 1))$. For many stars and sufficiently small f or large fluctuations $G(f) \simeq 1 - \frac{1}{2} f^2 \langle F^2 \rangle$, and the previous expression converges to a Gaussian distribution whose width $\propto m^{-1/2}$. This prescription was implemented numerically assuming $\mathcal{P}(F) \propto 10^{-2.5B \log_{10} F}$ with $B = 0.3$. Convolution of the predicted star histogram with Gaussian measurement noise and Gaussian cosmic background fluctuations can be included by multiplying $G(f)$ by a Gaussian. The effective beam size sets the maximum value of the apparent dN/dm in the confusion noise region. We are able to reproduce Fig. 7 very well, including the negative fluctuations and the transition from the confusion noise region to direct star detection. The result is robust in that the effective value of B measured at the bright end of the distribution is not altered by subtracting the mean value, and clipping with various N_{cut} has no effect on the value of B at the bright end. The apparent number of bright stars is about 10% larger than the input value, owing to the bias introduced by undetected stars of medium brightness near the detected bright stars.

We also want to know whether there is any feature of our processing algorithm that could produce a spurious residual fluctuation a . For this, we need a numerical simulation of the sky, including both stars and possible cosmic terms. We used the DIRBE star model of Arendt et al. (1998), who implemented the 96-component star population model of Wainscoat et al. (1992), including spatial distribution models for the disk, bulge, halo, ring and arm populations. These were evaluated using the K-band dN/dm for the central pixel of each patch, and a 2-dimensional

uniform random number generator, and the stars out to $K = 20$ were placed at the centers of the pixels in the map. The flux from each star was then distributed among 9 pixels according to the measured or assumed beam shape, using delta-function, uniform, and Gaussian beam profiles. If the correct beam profile is used, the simulated maps processed with our algorithms match the DIRBE histograms in each patch very well.

We also simulated CIB fluctuations, starting with Gaussian fluctuations in Fourier space with power spectrum $P(k) = k^{-1.3}$, as expected on the smallest DIRBE scales, and then multiplied by the top-hat beam window function determined in Sec. 3. The resultant field was then Fourier transformed to real space and normalized to the modeled cosmic variance, σ_{sky} . We added these maps to the simulated star fluctuation maps and examined the results.

As was discussed in Sec. 4.2, our clipping algorithm clips effectively about $\sim 1 \sigma$ below the nominal value of N_{cut} , because each star is seen in multiple pixels, each with its own noise fluctuations. Furthermore, according to Eq. (29), there should be no variation with $\text{cosec}|b|$ in the number of stars clipped in each patch if the star counts follow the same B over the relevant range of magnitudes. To test this we computed the effective $N_{\text{cut,eff}} = \sqrt{\frac{5}{3}N_{>}^{-1}}$ according to Eq. (29) assuming $B = 0.3$. The number of clipped stars, $N_{>}$, is half the number of clipped pixels since our mask has twice the beam area. The results are plotted against $\text{cosec}|b|$ in Fig. 15 for both the real sky and the model Galaxy. The data show that in the anti-center quadrants outside the Galactic plane, there is no trend with $\text{cosec}|b|$, and the effective values of N_{cut} have very small dispersion. For the real sky, the mean in this range is $N_{\text{cut,eff}} = 2.26$ and the dispersion is $\sigma_{\text{cut}} = [\langle N_{\text{cut,eff}}^2 \rangle - \langle N_{\text{cut,eff}} \rangle^2]^{1/2} = 0.06$. For the model sky, the mean $N_{\text{cut,eff}} = 2.27$, and the dispersion is 0.07. The effective N_{cut} is independent of the simulated beam properties.

We found a simple way to test the assumption of a plane parallel Galaxy. As Eq. (25) shows, the quantity $x^{-3}(dN/dm)|_x$ plotted against $m - 5 \log_{10} x$ should be independent of $x = \text{cosec}|b|$ and be equal to the counts at the Pole. We computed histograms for 14 patches of 64×64 pixels at $|b| > 20^\circ$, $|\beta_{\text{ecl}}| > 30^\circ$ and $90^\circ < l < 270^\circ$. The patches were clipped at $N_{\text{cut}} = 3.5$ and the average flux for the remaining pixels of each patch was subtracted from the map. The resultant

distribution of $x^{-3}dN/dm$ is plotted in Fig. 16 for K band, with Poisson error bars for those points that contain at least 25 pixels (or 5.5 stars). The figure confirms that the stars are distributed in a plane-parallel way for this data set, with $B \simeq 0.3$. The plot includes lines for the model Galaxy, with error bands. They agree with the observations within the errors except at the bright end, where the model is slightly low.

We simulated skies with a cosmic term of $\sigma_{\text{sky}} = 5 \text{ nWm}^{-2}\text{sr}^{-1}$ for the same 64×64 patches. The observations and the simulated model are plotted in Fig. 17, with fluxes measured in units of $\sqrt{C(0)}$. If all the fluctuations are due to stars drawn from a power law distribution of the same slope, then all of the patches should follow the same line on this diagram. The DIRBE data and the synthetic Galaxy model look nearly identical, and there is no noticeable difference between $\sigma_{\text{sky}} = 5 \text{ nWm}^{-2}\text{sr}^{-1}$ and 0. The DIRBE data and the models could be matched even better by adjusting the beam shape for the synthetic maps. The simulated confusion noise does not affect the amplitude and slope of the star counts at $m_K < 5.5$.

Using our simulated models we also tested the scaling of the amplitude of the residual variance at given N_{cut} as a function of the input isotropic component σ_{sky} . This is important because our clipping algorithm might remove both cosmic and star fluctuations in a complicated and possibly non-linear way. We find that even at $N_{\text{cut}} = 3.5$, the residual variance $C(0)$ is to good accuracy the sum of the variances from stars and the simulated CIB contribution. This shows that Eq. (31) is better justified than the other choices for extrapolating to $\text{cosec}|b| = 0$. The choice of beam shape - Gaussian, delta-function, or uniform - has no effect on the effective N_{cut} , but does lead to a systematic change in the residual $C(0)$, with the largest beam area having the highest variance.

Similarly, changing the size f_{size} of the lower envelope region used by the point source recognition algorithm has no affect on $N_{\text{cut,eff}}$, but leads to a systematic dependence of $C(0) \propto 1/f_{\text{size}}$. Clearly, the larger the value of f_{size} , the more diligently the algorithm recognizes point sources. We used $f_{\text{size}} = 5$, corresponding to about 5 DIRBE beams.

We can now predict what the Galactic star counts ought to be in order to reproduce the $C(0)$ vs. $x = \text{cosec}|b|$ relation found in the previous section. Combining Eqs. (25) and (26) shows that

for a plane-parallel model the star contribution to the fluctuation is related to dN_P/dm at the Pole via

$$x\sigma^2(x) = F_0^2 \int_{m_L - 5 \log_{10} x}^{\infty} 10^{-0.8y} \frac{dN_P}{dy} dy, \quad (34)$$

where F_0 is the zero magnitude flux; for Band 2 it is $6050 \text{ nWm}^{-2}\text{sr}^{-1}$ per DIRBE pixel. The lower magnitude for our clipping method is given by $m_L = -2.5 \log_{10}[f_m N_{\text{cut}} \sigma(x)/F_0]$. Here f_m is a factor accounting for the beam and the lower envelope used; based on the discussion in the previous paragraph we expect $f_m \sim 0.5 - 0.6$. Differentiating both sides of Eq. (34) leads to

$$\frac{dN_P}{dm} = 10^{0.4m} \frac{0.4 \ln 10}{f_m N_{\text{cut}} F_0} \frac{\partial[x\sigma^2(x)]/\partial x}{\partial[x^2\sigma(x)]/\partial x}. \quad (35)$$

Here the right-hand-side should be evaluated for x given by:

$$m(x) = -2.5 \log_{10}[f_m N_{\text{cut}} x^2 \sigma(x)/F_0]. \quad (36)$$

Eqs. (35), (36) form a closed set to determine the star counts required to reproduce the $\sigma(x)$. They thus provide an important consistency check between the measured effective N_{cut} , the $C(0) - x$ relation, and the star counts at the Galactic Poles. They also show whether the $\text{cosec}|b|$ -independent part of $C(0)$ can be produced by the observed stars.

We can measure the f_m factor by normalizing the recovered star counts to the DIRBE data at $m_K = 4$, where the confusion noise is negligible, and find $f_m \simeq 0.6$. The solid line in Fig. 7 shows the recovered star counts at the Pole from $C(0)$ given by Eq. (31) with $a = 0$ with parameters (A, p) taken from Table 1. The agreement between the star counts inverted from the observed $C(0) - x$ relation and the actual data is remarkably good, considering the statistical uncertainty in A, a and p , and given that all three ($C(0)$ vs. x , N_{cut} and dN_P/dm) were determined independently. The dashed line in Fig. 7 shows the star counts required to reproduce Eq. (30) with $a = 4.8 \text{ nWm}^{-2}\text{sr}^{-1}$ according to Eqs. (35), (36). The line overshoots the data by several standard deviations at $m_K > 5$ and shows that this value of a cannot be produced by the observed Galactic stars.

We can now use the simulated sky maps to test the extrapolations to $\text{cosec}|b| = 0$. We constructed simulated data for 384 patches of 32×32 pixels which contained both the K Band

Galaxy synthetic model, and a contribution from the CIB with σ_{sky} varying from 0 to 20 $\text{nWm}^{-2}\text{sr}^{-1}$. Processing the simulated maps with the standard algorithm, we find that the model without the CIB term is a good match to the DIRBE data at intermediate latitudes, but is significantly steeper as $\text{cosec}|b| \rightarrow 0$ at $|b| > 45^\circ$, and has a zero intercept within the statistical errors. On the other hand the simulated data curve at $|b| > 45^\circ$ flattens out for positive values of σ_{sky} .

We also tried fitting the simulated sky fluctuations to the observations, using $C(0) = A_m \sigma^2(\sigma_{\text{sky}}) + a_m$, and found the effective gain and offset A_m, a_m . This approach has the advantage of including all that is known about the geometrical shape of the Galaxy, since the simulated maps use the Wainscoat et al. (1992) shapes for the disk, bulge, halo, ring and arm. If the model includes a cosmic term of the correct amplitude, then we should find $A = 1$, $a_m = 0$. We find that for a model $\sigma_{\text{sky}} = 0$ the value of $A_m = 1.4 \pm 0.3$, consistent with unity, and the numbers for A_m for positive values of σ_{sky} are similar. We could achieve $A = 1$ by better modeling of the DIRBE beam size, since we have already shown that relationship.

We also confirm the values for the residual fluctuations a in Table 1. If the modeled sky has $\sigma_{\text{sky}} = 0$, we find $\sqrt{a_m} = 7.3^{+2.0}_{-2.8} \text{ nWm}^{-2}\text{sr}^{-1}$ in agreement with Table 1. Conversely, if we choose a model σ_{sky} similar to a in Table 1, then a_m should be consistent with zero. We find $a_m = 0$ with the 92% confidence level for $2.8 \text{ nWm}^{-2}\text{sr}^{-1} < \sigma_{\text{sky}} < 8.3 \text{ nWm}^{-2}\text{sr}^{-1}$ with the central value lying at $\sigma_{\text{sky}} = 5.2 \text{ nWm}^{-2}\text{sr}^{-1}$.

We can imagine only one possible feature in the DIRBE data processing that could lead to a false conclusion about the latitude dependence. We have shown that for a range of fixed beam size and shape, the sky models all predict a dependence of star fluctuations on latitude that extrapolates to zero fluctuations at zero $\text{cosec}|b|$. There is however some possibility that the effective beam size might depend on the line of sight and hence possibly on Galactic latitude. To explain the measurements, we would have to find an effect that systematically changes the effective beam area by an amount of the order of 30%, comparable to the fraction of the fluctuations at the Galactic pole that seem to be of cosmic origin.

The DIRBE team measured the actual beam size very carefully from transits of bright stars through the beam, and did not find a significant dependence of beam profile on time or direction. However, as noted elsewhere, the effective beam profile for measuring fluctuations depends on several other effects. The effective beam area is approximately $\Omega = 2\pi(\theta_{\text{beam}}^2/2 + \theta_{\text{pixels}}^2 + \theta_{\text{pointing}}^2)$, where θ_{beam} is the measured beam radius, θ_{pixels} is the rms radius of the pixels, and θ_{pointing} is the rms (vector) pointing error. The rms pixel size is $d_{\text{pix}}/6^{1/2} = 0.132^\circ$ for a square pixel of side d_{pix} , but for a rhombus of the same area and a 60° corner angle, it is increased by a factor of $(2/\sqrt{3})^{1/2} = 1.075$ to 0.142° . Ignoring pointing error, this increases the effective beam area by 3.2%, a negligible amount in this context. The measured DIRBE pointing error is 1.5 arcmin (1σ), and increases the effective beam area by a fixed 3.9%. If, however, the pointing error were much larger than indicated by the statistics of the residuals from the pointing solution fits, and in addition were strongly dependent on Galactic latitude, the effect could be important for us. The pointing solution was the subject of extraordinary scrutiny by the COBE team, and such errors would have been noticed. We conclude that the latitude fitting method is not subject to errors due to changes of the effective beam size with latitude.

4.6. Power spectrum

Although the dominant spatial structure of the near IR maps is simply the white noise of stars, it is interesting to see whether large scale averages could reveal a CIB component. We computed both power spectra and angular correlation functions, and the results are shown in Figs. 18 and 19. We describe the power spectra first.

We used 96 patches of 64×64 pixels (or $19^\circ \times 19^\circ$), and computed spatial power spectra without star clipping, and with $N_{\text{cut}} = 7$ and 5, leaving over 90% and 80% of the pixels remaining at high latitudes. Smaller N_{cut} left too few pixels for reliable power spectra, and showed significant effects of the masking. We computed power spectra for single bands and for the color-subtracted maps, $\delta_1 - \beta\delta_2$, with β evaluated for each patch according to Eq. (18). After each power spectrum was calculated, it was divided by the beam window function discussed in Sec. 3 to take out the

instrument signature. The fact that the power spectra are approximately flat confirms that stars are the dominant sources of fluctuations for $N_{\text{cut}} = 5$, and that the effective window function, accounting for pixelization, map distortion, beam smearing, and pointing errors, is correct.

The single band power spectra also show large-scale gradients produced by the Galactic structure. The amplitude of the power spectrum decreases with N_{cut} , but the overall shape does not change appreciably, indicating that the beam mask effects are negligible for these values of N_{cut} . The amplitudes of the power spectrum for all angular scales are too large, and the shape too wrong, to allow for detection of the CIB structure. However, for some patches at $N_{\text{cut}} = 5$ the spectrum is close to that expected from Table 1. For N_{cut} of 5 or more, we can not extrapolate these power spectra to $\text{cosec}|b| = 0$ for most of the scales probed by $P(q)$, and for smaller N_{cut} there are too few pixels left.

Fig. 18 shows the power spectrum for patch No. 7, at Galactic $(l, b) = (115^\circ, 61^\circ)$, and ecliptic $(\beta_{\text{Ecl}}, \lambda_{\text{Ecl}}) = (56^\circ, 163^\circ)$. In the single bands, the amplitude of the power spectrum decreases strongly after point source removal, but the shape remains approximately the same. The solid line in each panel shows the CIB signal according to Table 1, assuming that the CIB power spectrum has $P \propto q^{-1.3}$. This is a valid approximation for scales below one degree, but on large scales the power index of the CIB power spectrum may be different. The power spectrum of the foreground exceeds the estimated CIB by only a modest factor, particularly in Band 4. An instrument with a smaller beam might detect these fluctuations directly.

Color subtraction significantly reduces the foreground structure, as shown in Fig. 18. Without clipping, we find a reduction by a factor of ~ 30 between adjacent bands, although the spectra are still flat from star fluctuation noise. Galactic stars are dominant in Band 4 and zodiacal and cirrus emission are dominant in Band 5, so these bands are not strongly correlated. For this patch, color subtraction of Bands 4 and 5 shows structure dominated by cirrus dust, which has $P \propto k^n$ with a steep $n = -2$ to -3 ; see Sec. 5. The solid line in the lower panels shows the estimated small-scale CIB between Band 1 and Band 2 with logarithmic slope of -1.3 and $C(0)$ taken from Table 1. In Bands [2 – 3], we plot $\sqrt{C(0)} = 2 \text{ nWm}^{-2}\text{sr}^{-1}$.

For lower values of N_{cut} and $q^{-1} > 1^\circ$, the amplitude of $P(q)$ is comparable to that expected from the CIB according to Table 1. Furthermore, the slope of the power spectrum for this patch flattens significantly in the color-subtracted maps, and at some scales and bands approaches the logarithmic slope expected from the CIB. However, inspection of the power spectra shows that even in the color-subtracted maps, we do not detect a cosmological signal for $N_{\text{cut}} \geq 5$. The spectra are all consistent with the white-noise stellar distribution and large-scale Galactic gradients. To check for a cosmological power spectrum consistent with Table 1 we would have to clip to much lower levels of N_{cut} where beam masking problems prevent reliable determination of the power spectrum.

For $N_{\text{cut}} < 5$, it is better to compute angular correlation functions, which are unbiased by masking effects, even for $N_{\text{cut}} = 3.5$ where less than 50% of pixels remain. We evaluated $C(\theta) = \langle \delta F(\mathbf{x} + \theta) \delta F(\mathbf{x}) \rangle$, averaging over the remaining pairs of pixels separated by angular distance θ . (The points at different θ are not statistically independent of each other. For $N_{\text{cut}} = 7$ and 5 the correlation function is that of white noise, a delta function at zero lag, with a level consistent with the power spectrum plotted in Fig. 18. It remains close to the zero-lag value on scales inside the beam, $\theta < 0.5^\circ$ and rapidly drops to very small (positive or negative) numbers on larger scales. For $N_{\text{cut}} = 3.5$ for patches with low values of $C(0)$ the correlation function flattens significantly, which would be consistent with CIB structure at the levels of Table 1. Fig. 19 shows the correlation function for Patch 7 at $N_{\text{cut}} = 3.5$, for 10 bins of 1 degree width. The straight line illustrates the slope of a CIB correlation function $\propto \theta^{-0.7}$. The correlation function amplitude and slope are consistent with Table 1 and a CIB interpretation. Large-scale gradients in the star and dust populations are responsible for the positive correlation function at very large angles.

A further comparison between the results in Table 1 and the power spectrum analysis can be made in the following way. For $N_{\text{cut}} = 5$ at each angular scale q^{-1} , we evaluate the minimal value of $P(q)$ for all the patches, and plot the value of a typical fluctuation, $\sqrt{q^2 P(q)/2\pi}$, versus $\theta = \pi/q$ in Fig. 20. The slope of the data is roughly that of white noise, $\sqrt{q^2 P(q)/2\pi} \propto q$, implying that

we are still seeing Galactic stars. The upper limits over angular scales of $2^\circ < \theta < 15^\circ$ are:

$$\delta F_{rms}(\theta) \leq A \left(\frac{\theta}{5^\circ}\right)^{-1}, \quad (37)$$

with $A = 6, 2.5, 0.8, 0.5$ nWm⁻²sr⁻¹ for Bands 1 to 4 respectively. The process of finding an all-sky minimum of $P_2(q)$ produces a very smooth curve whose uncertainties are predominantly systematic. These are strong constraints on galaxy evolution. The shaded areas represent the power spectra according to Table 1, assuming that the CIB $P(q) \propto q^{-1.3}$. Table 1 is consistent with the upper limits given by Eq. (37), except in Band 4. In Band 4, Table 1 would require a small scale for the turn-over in the CIB power spectrum, implying that much of it comes from high redshifts.

5. Results in mid- to far-IR Bands

5.1. Foregrounds and $C(0)$ analysis

At wavelengths greater than 10 μm , dust in the Solar system and the Galaxy produce most of the foreground emission. These sources are smooth on small scales, so do not necessarily prevent detection of CIB fluctuations. Odenwald, Newmark and Smoot (1998) detected < 100 nearby galaxies in the DIRBE data at wavelengths greater than 10 μm , but with the exception of M31 and the Large and Small Magellanic clouds, the galaxies are unresolved. Because there are few discrete sources in the mid and far-IR DIRBE data, we can clip the DIRBE maps to lower values of N_{cut} and keep the same number of pixels as for the near-IR bands.

Clipping to low values of N_{cut} would remove some fluctuations in the CIB as well as the foreground. If the CIB zero-lag signal were as high as the upper limit found in the maps, clipping at $N_{\text{cut}} = 2, 2.5$ or 3 levels would decrease the real $C(0)$ by 20%, 10% and 0.001% respectively. Given that we find only upper limits, clipping down to $N_{\text{cut}} = 2$ is safe but lower levels would require interpretation.

Fig. 21 shows histograms of the number of pixels remaining in each patch of 32×32 pixels

after removing point sources with $N_{\text{cut}} = 2$. Because of the extended nature of the foreground emission in these bands, we removed large-scale gradients first, using polynomials of order up to 4. Fig. 22 shows the variation of the residual $C(0)$ with $\text{cosec}|b|$ at $N_{\text{cut}} = 2$ for $90^\circ < l < 270^\circ$. A significant fraction of the foreground emission still comes from the zodiacal light, even after subtraction of the DIRBE zodiacal light model, and contributes to the large scatter in the plots. Fig. 22 also shows the dependence of $C(0)$ on Galactic latitude for the 111 patches that also have Ecliptic latitude $|\beta_{\text{Ecl}}| > 25^\circ$. The scatter is reduced but not enough to extrapolate to $\text{cosec}|b|=0$.

In Bands 5 and 6 there is only a weak dependence on b , and the amplitude of the typical fluctuations seen in these bands changes by only $\sim 50\%$ between $\text{cosec}|b| = 1$ and 3, showing approximate isotropy for $|b| \geq 20^\circ$. We interpret the lowest values of $\sqrt{C(0)}$ as upper limits on the CIB fluctuations. They are slight improvements over Paper II, and are shown in Table 2.

In Bands 7 and 8 the dependence on Galactic latitude is more prominent. Extrapolation to $\text{cosec}|b| = 0$ with Eq. (30) gives values of a in agreement with the lowest $\sqrt{C(0)}$ shown in Table 2, but with significant error bars. Therefore we again interpret the derived $C(0)$ as upper limits on the CIB fluctuations. The slope of $C(0)$ with Galactic latitude is consistent with a plane parallel Galaxy distribution, i.e. $\sqrt{C(0)} \propto \text{cosec}|b|$. The fluctuations are approximately proportional to the total brightness.

The color diagrams at these wavelengths are not as clean as in the near-IR. In many patches no color correlations between the adjacent bands exist, and the color indices show large variations across the sky. Local variations in the parameters of the Galactic and solar system dust (e.g. density and temperature) are expected on large angular scales. No improvement in the CIB limits was achieved with mid-IR color subtraction.

5.2. Mid- and Far-IR Power Spectra

We computed power spectra for the same 96 patches of 64×64 pixels used for the near IR bands. Both single band power spectra and color-subtracted maps show a weak decrease with

clipping threshold, a consequence of the extended character of the foreground emission. The reduction of the foreground with the color subtraction is not as large as in the near-IR bands. In order to preserve information about $P(q)$ at all angular scales, no gradients were removed before power spectrum analysis.

The power spectra have a shape typical of the known cirrus distribution (cf. Gautier et al. 1992). The spectrum $P(q)$ is steep: $P(q) \propto q^{-n}$ with $n \simeq (2.5 - 3)$. This is consistent with little small scale structure and, hence, no strong dependence in the resultant $C(0)$ on N_{cut} . It is also consistent with the power spectrum of cirrus emission measured on arc-minute and degree scales (Gautier et al. 1992; Wright 1998). Fig. 23 shows power spectra for the same Patch 7 used in the near-IR analysis. It shows the steep power spectrum typical of the cirrus distribution with $P(q) \propto q^{-3}$ for most of the scales. Note that some of the fluctuations at 12 and 25 μm can be due to errors in modeling the zodiacal light.

As in the near-IR analysis, we evaluated the minimal values of $P(q)$ for each angular scale q^{-1} across the entire sky. Fig. 23 shows these minimal values of the fluctuation $\sqrt{q^2 P(q)/2\pi}$ as a function of angular scale π/q . The minimal values come close to, but are not as small as, those in Table 2, which were evaluated at $N_{\text{cut}} = 2$ after gradient subtraction. Even in the patches with the least fluctuations, the power spectrum is still as steep as $P \propto q^{-2}$, leaving the fluctuation $\sqrt{q^2 P(q)/2\pi} \simeq \text{const}$. This is indicative of cirrus emission in all areas of the sky. Infrared sky surveys with higher angular resolution should be able to reduce this contribution, and possibly uncover the CIB fluctuations.

6. Conclusions

Fig. 24 summarizes our results. At 1-5 μm , we find a positive residual fluctuation by extrapolating $C(0)$ to zero $\text{cosec}|b|$. Based on detailed numerical and analytic models, this residual is not likely to originate from the Galaxy, our clipping algorithm, or instrumental noise. We conclude that this extra variance may result from structure in the CIB. The variance found in

this way from individual DIRBE Bands 1-4 is plotted with diamonds, with 92% uncertainty levels from Fig. 13. The results for color-subtracted maps are plotted with triangles at wavelengths halfway between the bands used. We find a positive residual in the color-subtracted map [1-2] between Bands 1 and 2, but not in other color subtracted maps. The color-subtracted map [1-2] has a unique color of $\beta_{12} \simeq 2$ with little variation across the sky and the limit measures $[(\delta F_1 - 2\delta F_2)^2]^{1/2}$. Taken at face value, these high values of the near-IR CIB fluctuations, if produced by evolving normal galaxy populations, would require substantial CIB fluxes. These would have to be above the estimates from the K-band galaxy counts, but are below the upper limits found by Hauser et al. (1998). The upper limits on CIB fluctuations at 10 - 100 μm are plotted with arrows, and are below $1 \text{ nWm}^{-2}\text{sr}^{-1}$, with $\sqrt{C(0)} < 0.5 - 0.7 \text{ nWm}^{-2}\text{sr}^{-1}$ at 25 μm . These limits are lower than those in Paper II and imply strong constraints on how and when the early galaxies formed and evolved.

On larger scales, $2^\circ < \theta < 15^\circ$, we obtain upper limits on the CIB fluctuations from the all-sky power-spectrum analysis: $(\theta/5^\circ) \times \delta F_{\text{rms}}(\theta) < 6, 2.5, 0.8, 0.5 \text{ nWm}^{-2}\text{sr}^{-1}$ in Bands 1-4 respectively. These limits, when taken in conjunction with our possible detection of the zero-lag CIB signal, limit the turn-over scale in the spectrum of the primordial density field to not much more than $\sim 100h^{-1}\text{Mpc}$.

We fully recognize the difficulty of finding small fluctuations in the presence of larger fluctuations from foregrounds. While we have found no local explanation for our results, it is still quite possible that the fluctuations are not of cosmic origin, but come from some fault of the instrument, the data processing, or an unexpected feature of the Galactic foreground. The best way to resolve this uncertainty is to get better data, such as from a higher resolution sky survey with exceptionally good attention to flat fielding. This may be possible with satellites like SIRTf or the proposed NGSS, or even from 2MASS data or rocket data.

We acknowledge support from the NASA Long Term Space Astrophysics grant 399-20-61-02. We particularly thank the COBE DIRBE team, led by the principal investigator Michael Hauser and by Thomas Kelsall, for developing an exceptionally well calibrated and stable instrument, and

for producing public data archives with the complex zodiacal light foreground models removed. We have benefited greatly from conversations with Richard Arendt on applications of star models to the DIRBE data and for a careful reading and constructive comments on the manuscript of this paper. Our special thanks go to Tom Jarrett for providing the 2MASS star counts data. We thank the referee, Michael Vogeley, for careful reading of the paper.

REFERENCES

- Arendt, R. et al. 1998, Ap.J., **508**,74.
- Bahcall, J. and Soneira, R., 1980, Ap.J.Suppl, **44**, 73.
- Baugh, C. & Efstathiou, G. 1993, MNRAS, **265**, 145.
- Beichman, C.A. 1996, in “Diffuse Infrared Radiation and the IRTS”, eds. Okuda, H., Matsumoto, T. and Roellig, T., p.82.
- Beichman, C.A. & Helou, G. 1991, Ap.J., **370**, L1.
- Boggess, N. et al. 1992, Ap.J., **397**, 420.
- Bond, J.R., Carr, B.J. and Hogan, C. 1986, Ap.J., **306**, 428.
- Chandrasekhar, S. 1954, in “Noise and stochastic processes”, ed. N. Wax, Dover.
- Cowie, L. et al. 1994, Ap.J., **434** , 114.
- Djorgovski, G. et al. 1995, Ap.J., **438**, L13.
- Dwek, E. et al. 1998, Ap.J., **508**,106.
- Elias, J.H. 1978, A.J., **83**, 791.
- Fall, S.M., Charlot, S. & Pei, Y.C. 1996, Ap.J., **464**, L43.
- Fixsen, D.J., Dwek, E. , Mather, J.C., Bennett, C.L., & Shafer, R.A. 1998, Ap.J., **508**, 123.
- Franceschini, A. et al. 1991, Ap.J.Suppl., **89**, 285.
- Gautier, N. et al. 1992, A.J., **103**, 1313.
- Hauser, M. et al. 1998, Ap.J.,**508**, 25.
- Hacking, P.B. and Soifer, B.T. 1991, Ap.J., **367**, L49.
- Jarrett, T. 1998, IPAC/Caltech, private communication.
- Jimenez, R. & Kashlinsky, A. 1999, Ap.J., **511**, 16. (astro-ph/9802337).
- Kashlinsky, A. 1998, Ap.J., **492**, 1.

- Kashlinsky, A., Mather, J., Odenwald, S. and Hauser, M. 1996, Ap.J., **470**, 681. (Paper I)
- Kashlinsky, A., Mather, J., and Odenwald, S. 1996, Ap.J., **473**, L9. (Paper II)
- Kelsall, T. et al. 1998, Ap.J., **508**, 44.
- Loveday, S. et al. 1992, Ap.J., **390**, 338.
- Lilly, S. et al. 1996, Ap.J., **460**, L1.
- Lin, H. et al. 1996, Ap.J., **464**, L60.
- Maddox, S. et al. 1990, MNRAS, **242**, 43P.
- Malkan, M.A. and Stecker, F. 1998, Ap.J., **496**, 13.
- Martin, C. and Bowyer, S. 1989, Ap.J., **338**, 677.
- Mihalas, D. and Binney, J. 1981, “Galactic Astronomy”, Freeman & Co., San Francisco.
- Minezaki, T. et al. 1998, A.J., **115**, 229.
- Moore, B. et al. 1994, MNRAS, **269**, 742.
- Odenwald, S., J. Newmark, & Smoot, G. 1998, Ap.J., **500**, 554.
- Partridge, B. & Peebles, P.J.E. 1967, Ap.J., **148**, 377.
- Peebles, P.J.E. 1980, Large Scale Structure of the Universe, Princeton University Press.
- Picard, A. 1991, Ap.J., **368**, L7.
- Saunders, W. et al. 1991, Nature, **349**, 32.
- Saunders, W. et al. 1992, MNRAS, **258**, 134.
- Shectman, S. 1973, Ap.J., **179**, 681.
- Shectman, S. 1974, Ap.J., **188**, 233.
- Shectman, S. et al. 1996, Ap.J., **470**, 172.
- Silverberg, R.F. et al. 1993, Proc. SPIE, **2019**, 180.
- Stecker, F., Puget, J-L., & Fazio, G.G. 1977, Ap.J., **214**, L51.

- Vogeley, M. 1998, astro-ph 9711209.
- Wainscoat, R.J., et al. 1992, Ap.J.Suppl., **83**, 111.
- Wang, B. 1991, Ap.J., **374**, 465.
- Weiland, J. et al. 1998, DIRBE Explanatory Supplement, http://www.gsfc.nasa.gov/astro/cobe/dirbe_exsup.html
- Wright, E.L. 1998, Ap.J., **496**, 1.
- Yoshii, Y. & Takahara, F. 1988, Ap.J., **326**, 1.

Fit	Band 1 1.25 μm	Band 2 2.2 μm	Band 3 3.5 μm	Band 4 4.9 μm	Band 1-2	Band 2-3	Band 3-4
$\sqrt{C(0)} = a + Ax^p$							
a	$12.5^{+4.3}_{-5.7}$	$4.8^{+1.8}_{-2.4}$	$1.9^{+0.6}_{-0.7}$	$2.0^{+0.2}_{-0.2}$	$6.7^{+1.6}_{-2.5}$	--	$1.4^{+1.2}_{-1.6}$
p	$2.15^{+0.41}_{-0.41}$	$2.18^{+0.41}_{-0.41}$	$2.31^{+0.45}_{-0.45}$	$2.79^{+0.61}_{-0.58}$	$1.92^{+0.55}_{-0.54}$	--	1.47
$C(0) = a^2 + A^2x^{2p}$							
a	$15.5^{+3.7}_{-7.0}$	$5.9^{+1.6}_{-3.7}$	$2.4^{+0.5}_{-0.9}$	$2.0^{+0.25}_{-0.5}$	$7.6^{+1.2}_{-2.4}$	--	
p	$1.78^{+0.27}_{-0.27}$	$1.79^{+0.28}_{-0.29}$	$1.89^{+0.33}_{-0.33}$	$2.03^{+0.90}_{-0.78}$	$1.49^{+0.34}_{-0.33}$	--	1.23
$\sqrt{C(0)} = a + \sum_{i=1}^2 A_i x^i$							
a	14.9 ± 5.4	5.6 ± 2.2	2.5 ± 1.2	2.7 ± 1.2	6.6 ± 0.8	--	0.9 ± 0.9
$\sqrt{C(0)} = a \exp(Ax)$							
a	9.7 ± 0.6	3.7 ± 0.2	1.3 ± 0.1	1.3 ± 0.1	5.3 ± 0.2	3.6 ± 0.2	1.5 ± 0.1
$x = [\ln \sqrt{C(0)} - \ln a] / A$							
a	8.8 ± 1.3	3.3 ± 0.3	1.1 ± 0.1	0.8 ± 0.1	4.8 ± 0.6	1.8 ± 0.4	1.2 ± 0.1
Summary							
a	$15.5^{+3.7}_{-7.0}$	$5.9^{+1.6}_{-3.7}$	$2.4^{+0.5}_{-0.9}$	$2.0^{+0.25}_{-0.5}$	$7.6^{+1.2}_{-2.4}$	--	

Note: $x = \text{cosec}[b]$

Table 1: Limits on a in $\text{nWm}^{-2}\text{sr}^{-1}$; the range corresponds to 92% confidence levels.

	Band 5	Band 6	Band 7	Band 8
	12 μm	25 μm	60 μm	100 μm
$\sqrt{C(0)}$	1.0	0.5	0.8	1.1

Table 2: Upper limits on $[C(0)]^{1/2}$ in $\text{nWm}^{-2}\text{sr}^{-1}$ for Bands 5-8.

Fig. 1: (a) Left: Linear scales of 0.5° in Eq. (12) vs. z . The minimal scale is almost independent of cosmology. (b) Right: $\Delta(k) \equiv (R_H^{-1} k^2 P_3(k; 0))^{1/2}$ vs. k for APM spectrum. The CIB minimal relative fluctuations on the DIRBE beam scale are $\sim \Delta$ at the minimal value of the linear scale.

Fig. 2: Window function and beam profile for DIRBE Band 1 beam. Plus signs show embedding in a 256^2 pixel field, asterisks 512^2 pixels, and diamonds 1024^2 pixels. Solid line is a top-hat profile with a beam radius of $\vartheta = 0.4^\circ$.

Fig. 3: Histogram of pixels surviving clipping at $N_{\text{cut}} = 3.5$ in the near-IR DIRBE bands for 384 patches of 32×32 pixels. Solid line is Band 1, dotted Band 2, dashed Band 3, and dashed-dotted Band 4.

Fig. 4: Histograms of color indices β from Eq. (18) for 384 patches. Thin solid lines are all-sky; thick lines are patches with $|b| > 20^\circ$.

Fig. 5: $\sqrt{C(0)}$ vs. $\text{cosec}|b|$ for Bands 1-4 and $N_{\text{cut}} = 3.5$.

Fig. 6: Same as Fig. 5 but for color subtracted maps.

Fig. 7: K band dN/dm and DIRBE pixel histogram for 128^2 pixels at NGP. Flux F is absolute value of deviation from mean of patch after clipping with $N_{\text{cut}} = 3.5$, measured in $\text{nWm}^{-2}\text{sr}^{-1}$. Positive deviations are + signs, diamonds negatives. Poisson error bars for DIRBE data assume 4.5 DIRBE pixels per star. Dotted lines are a Gaussian fit to data after clipping, and a 10% lower dispersion. Dash-dots are positive pixels remaining after clipping and dash-dot-dot-dot shows remaining negative pixels. Solid line shows counts inverted according to Eqs. (35) and (36) from Eq. (31) without an isotropic component; long dashes are inverted counts if a comes from stars. Filled triangles are differential counts from Elias (1978) NGP measurements. Filled circles are differential NGP counts from 2MASS (Jarrett 1998). Open triangles are cumulative 2MASS counts multiplied by $0.3 \ln 10$ to convert to differential counts for $dN/dm \propto 10^{0.3m}$. Filled diamonds with error bars are South Galactic Pole counts from Fig. 1 of Minezaki et al. (1998).

Fig. 8: Longitude dependence of $\sqrt{C(0)}$ for individual DIRBE bands at various Galactic latitudes. The increase of fluctuations towards the Galactic Center can be seen for any Galactic latitude.

Fig. 9: Same as Fig. 8 only for color-subtracted maps.

Fig. 10: Plots of $\sqrt{C(0)}$ vs. $\text{cosec}|b|$ for J, K, L, M bands for $90^\circ < l < 270^\circ$. Solid lines are fits of Eq. (31) using data for $|b| > 20^\circ$.

Fig. 11: Same as Fig. 10 for color-subtracted maps.

Fig. 12: Histogram of fit residuals from Eq. (30) for Band 2 $\delta_{\text{fit}}^2 = [(C(0) - a^2 - A^2 \text{cosec}^{2p}|b|)/C(0)]^2$ in units of σ_0 .

Fig. 13: 92% confidence limits on J, K, L, M and J-K for the fits to Eq. (31). The plus sign is the most likely value of (a, p) from Eq. (31).

Fig. 14: Scatter diagram for fit residuals $\delta_{\text{fit}} \equiv [\sqrt{C(0)} - \sqrt{C_{\text{fit}}(0)}]/\sqrt{C(0)}$ for Eq. (31) for Band 2 versus l and b .

Fig. 15: Effective clipping N_{cut} vs. $\text{cosec}|b|$, according to Eq. (29) for $p = 2$ or $B = 0.3$. Left is DIRBE data and right is simulated Galaxy model.

Fig. 16: K-band DIRBE star counts in coordinates where a plane-parallel Galaxy would be a single line; $x = \text{cosec}|b|$. Data are for 64×64 pixel patches with $|b| \geq 20^\circ$ and $90^\circ < l < 270^\circ$, with Poisson errors shown for $N_{\text{pix}} \geq 25$. Confusion noise affects counts at $m_K > 5.5$. Lines show the model Galaxy: solid is mean $x^{-3}dN/dm$ and dashes are the ± 1 -sigma spread.

Fig. 17: K-band star counts in the 64×64 patches outside the Galactic disk and away from the center, as a function of the absolute value of the flux deviation from the mean in units of $\sqrt{C(0)}$, for $N_{\text{cut}} = 3.5$. Left shows DIRBE data and right shows the simulated Galaxy and a CIB fluctuation of $\sigma_{\text{sky}} = 5 \text{ nWm}^{-2}\text{sr}^{-1}$ from Table 1. Plus signs are for negative F and diamonds for positive F ; they overlap for small $|F|$.

Fig. 18: Near IR power spectra for Patch 7, well above the Galactic and Ecliptic planes. Plus

signs are before point source removal, asterisks show $N_{\text{cut}} = 7$, and diamonds show $N_{\text{cut}} = 5$. Solid lines show $P(q)$ expected if the CIB power spectrum scales as $q^{-1.3}$ for a in Table 1.

Fig. 19: Angular correlation function evaluated for Patch 7 for $N_{\text{cut}} = 3.5$. The zero-lag value is plotted at $\theta = 0.15^\circ$, and numbers below $0.1 \text{ nW}^2\text{m}^{-4}\text{sr}^{-1}$ are not shown. The filled circle shows a from Table 1, normalizing a CIB correlation function with $C(\theta) \propto \theta^{-0.7}$. Diamonds show the absolute value of the correlation function in the negative range.

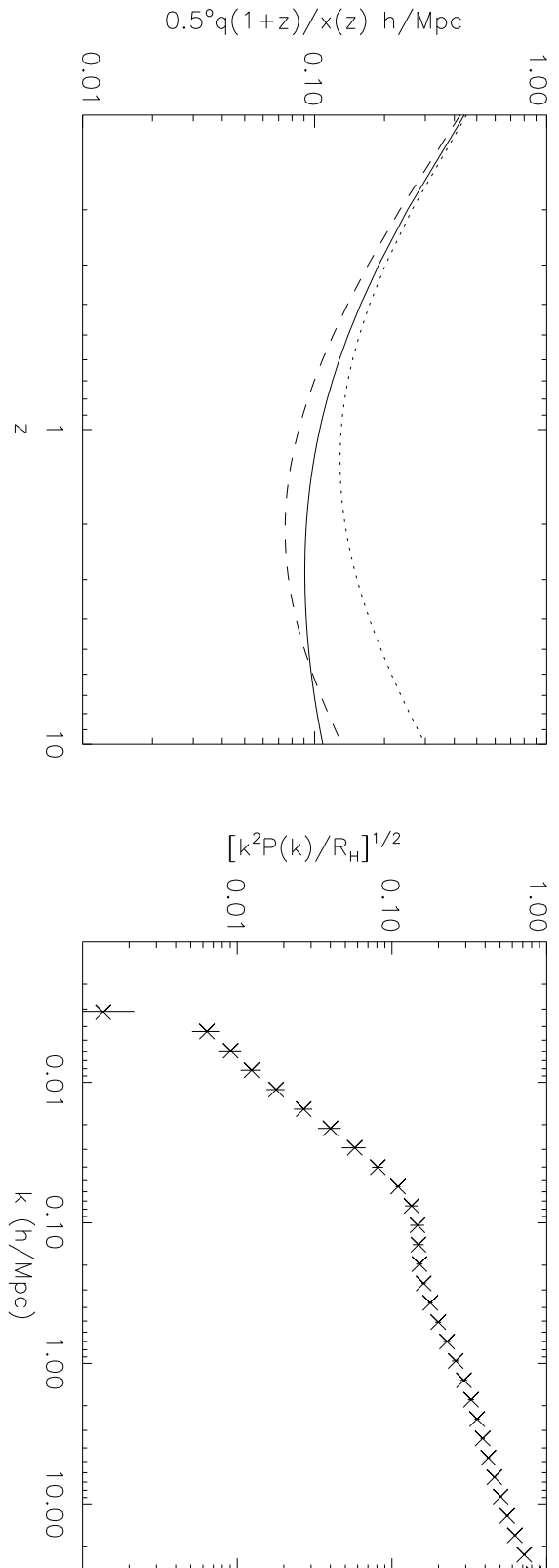
Fig. 20: All-sky minimum fluctuation $\sqrt{q^2 P(q)/2\pi}$ versus π/q . Shaded areas show the range expected from Table 1, assuming the CIB power spectrum scales as $q^{-1.3}$.

Fig. 21: Histogram of pixels surviving clipping at $N_{\text{cut}} = 2$ in the mid- to far-IR DIRBE bands for 384 patches of 32×32 pixels. Solid line is Band 5, dots Band 6, dashes Band 7, and dash-dots Band 8.

Fig. 22: $\sqrt{C(0)}$ vs. $\text{cosec}|b|$ for Bands 5-8 and $N_{\text{cut}} = 2$. Top panels are $90^\circ < l < 270^\circ$. Lower panels are $90^\circ < l < 270^\circ$ and $|\beta_{\text{Ecl}}| > 25^\circ$.

Fig. 23: Upper panels are near-IR power spectra in for Patch 7. Lower panels are all-sky minimum fluctuations $\sqrt{q^2 P(q)/2\pi}$ plotted vs. the scale π/q . Plus signs are without clipping, asterisks show $N_{\text{cut}} = 7$, and diamonds show $N_{\text{cut}} = 5$.

Fig. 24: Summary. Diamonds are values for a with 92% uncertainties from Table 1. Triangles are for the color subtracted maps, shown at the mean wavelength for the two bands. The 1 – 2 limits are the left triangle and 3 – 4 the right. Dashes with arrows are upper limits in Bands 4-8.



z

Fig. 1.—

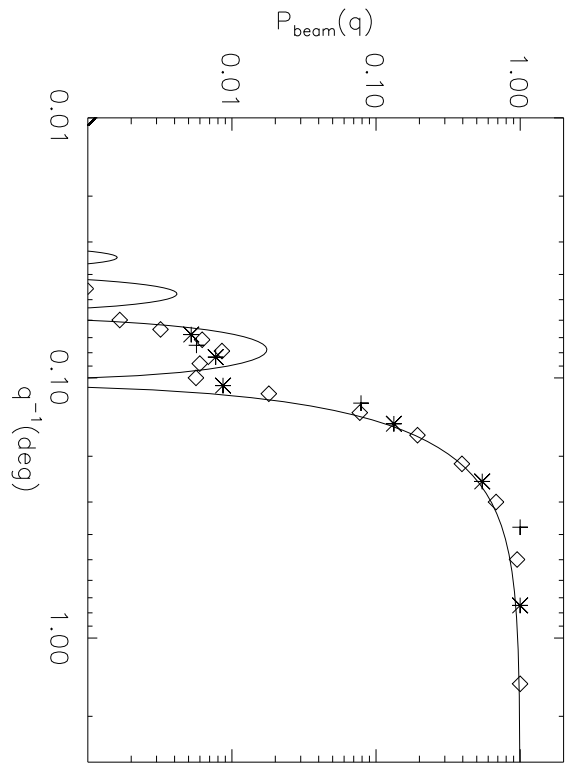


Fig. 2.—

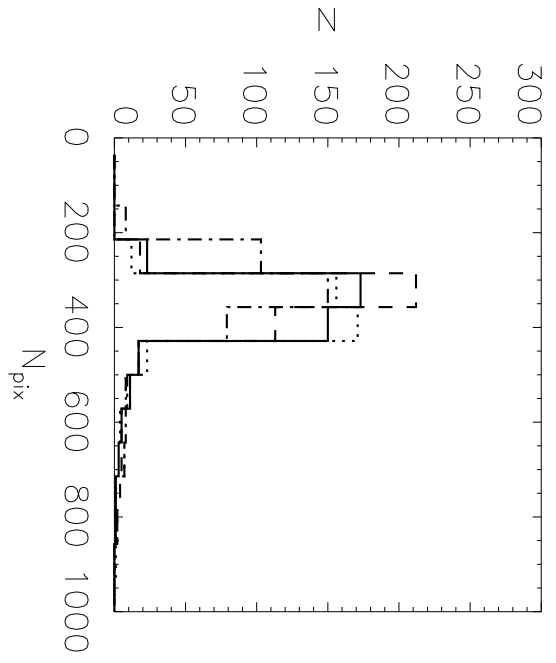


Fig. 3.—

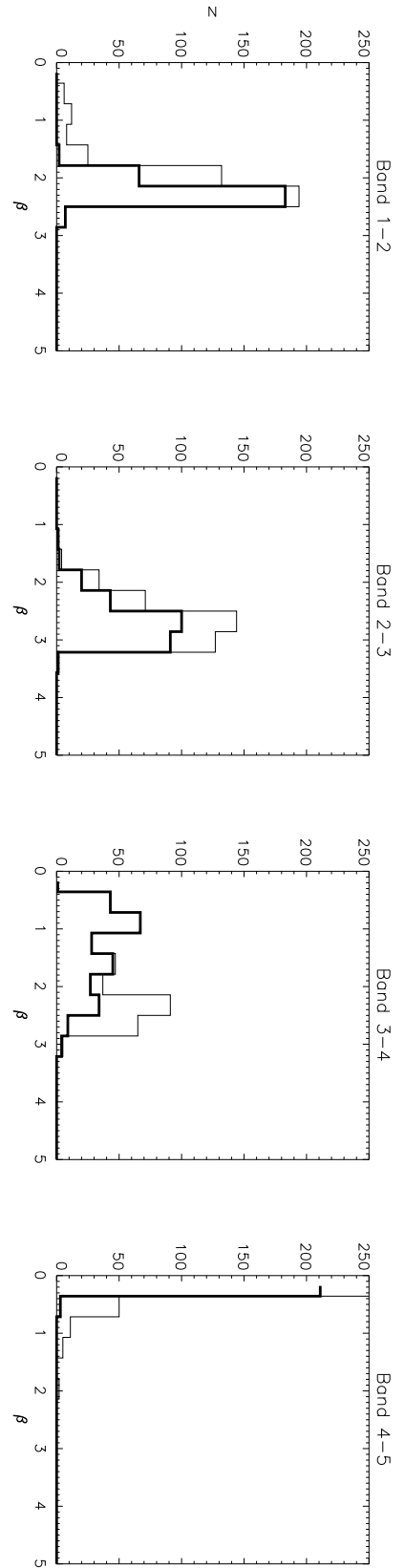


Fig. 4.—

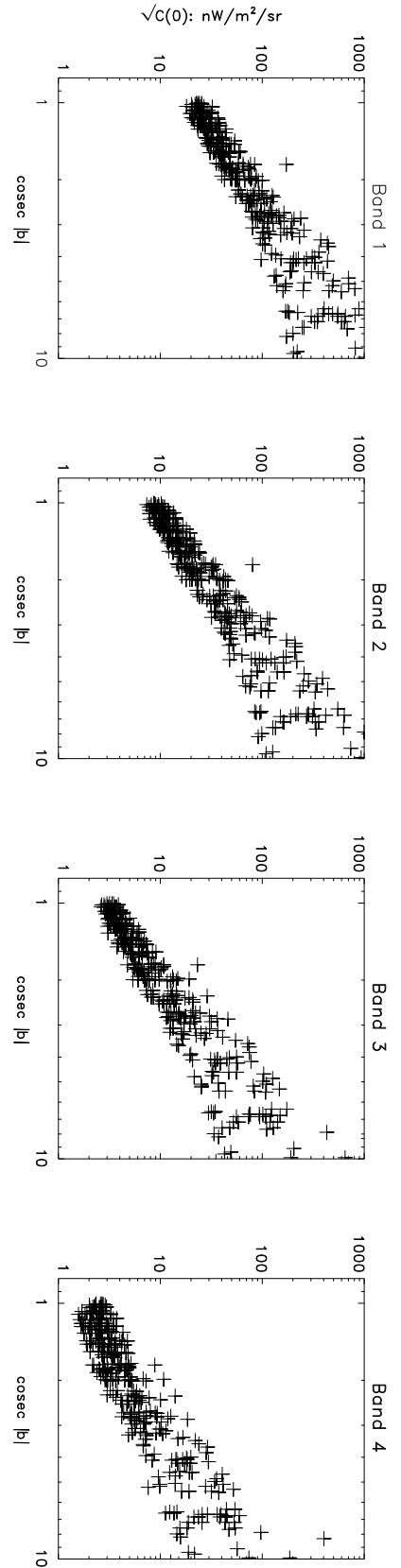


Fig. 5.—

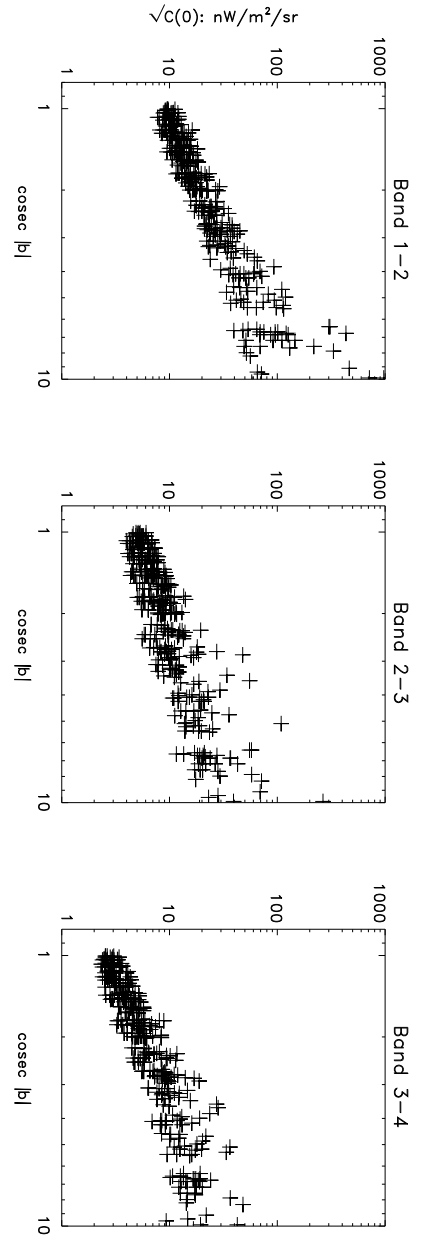


Fig. 6.—

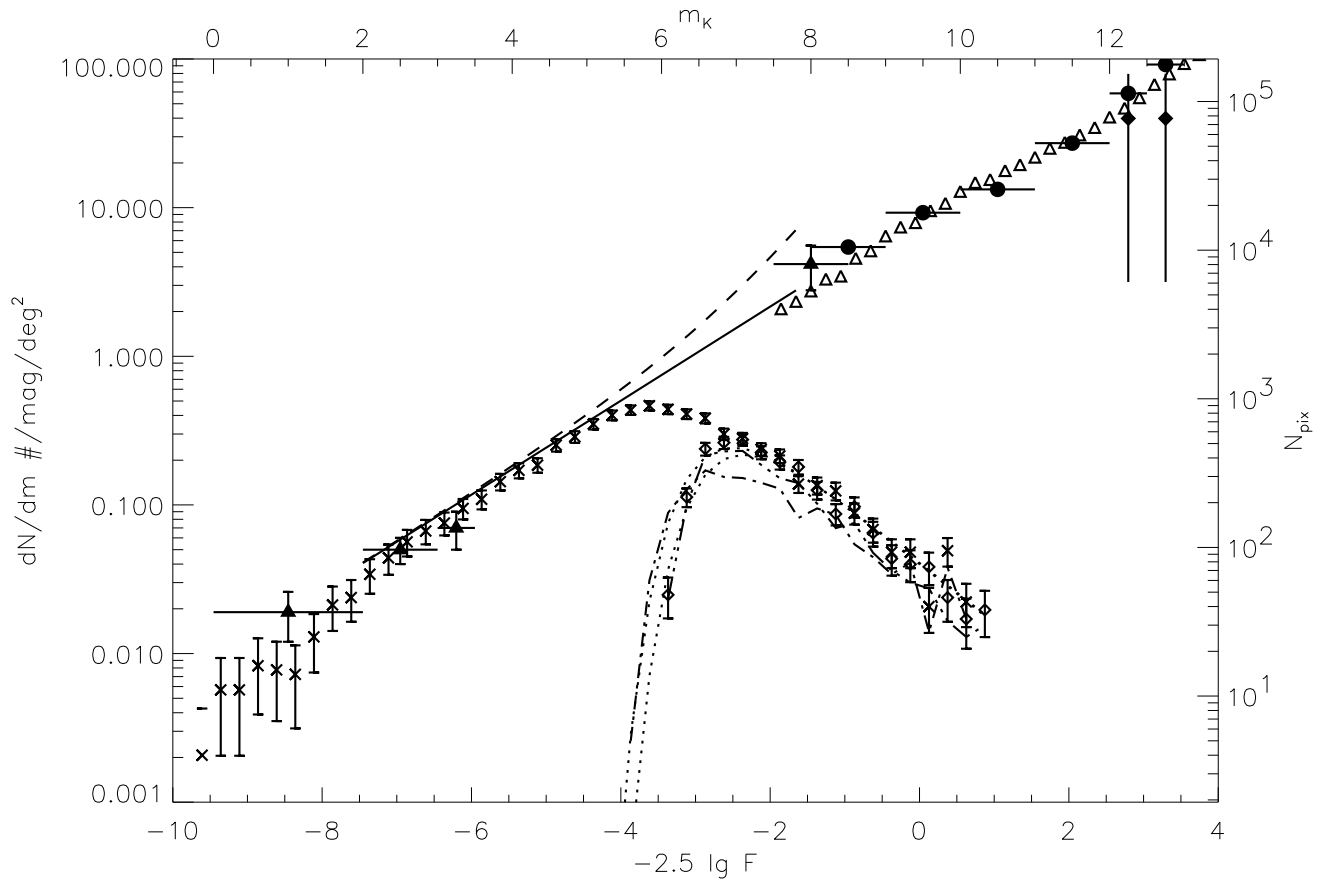


Fig. 7.—

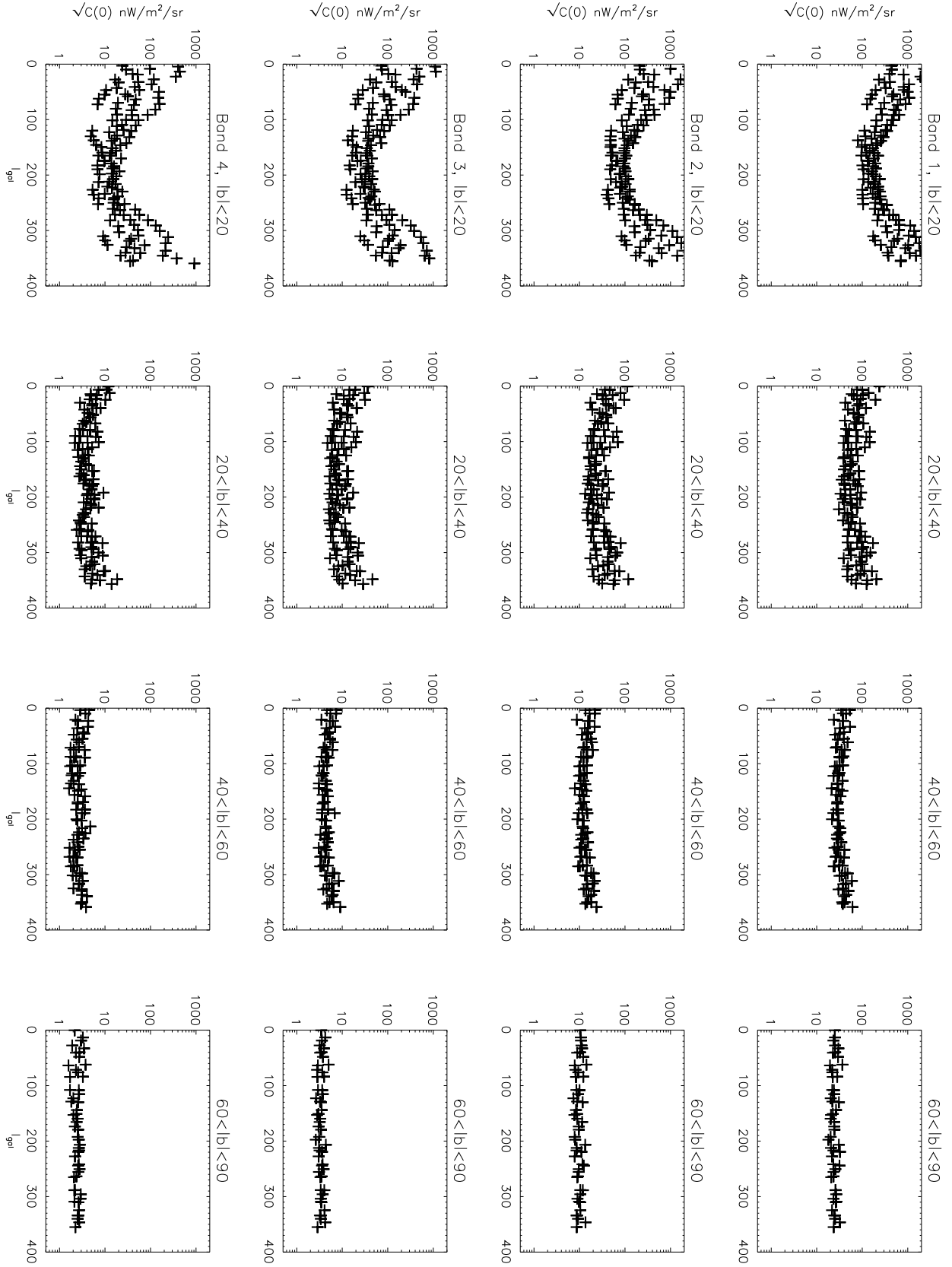


Fig. 8. —

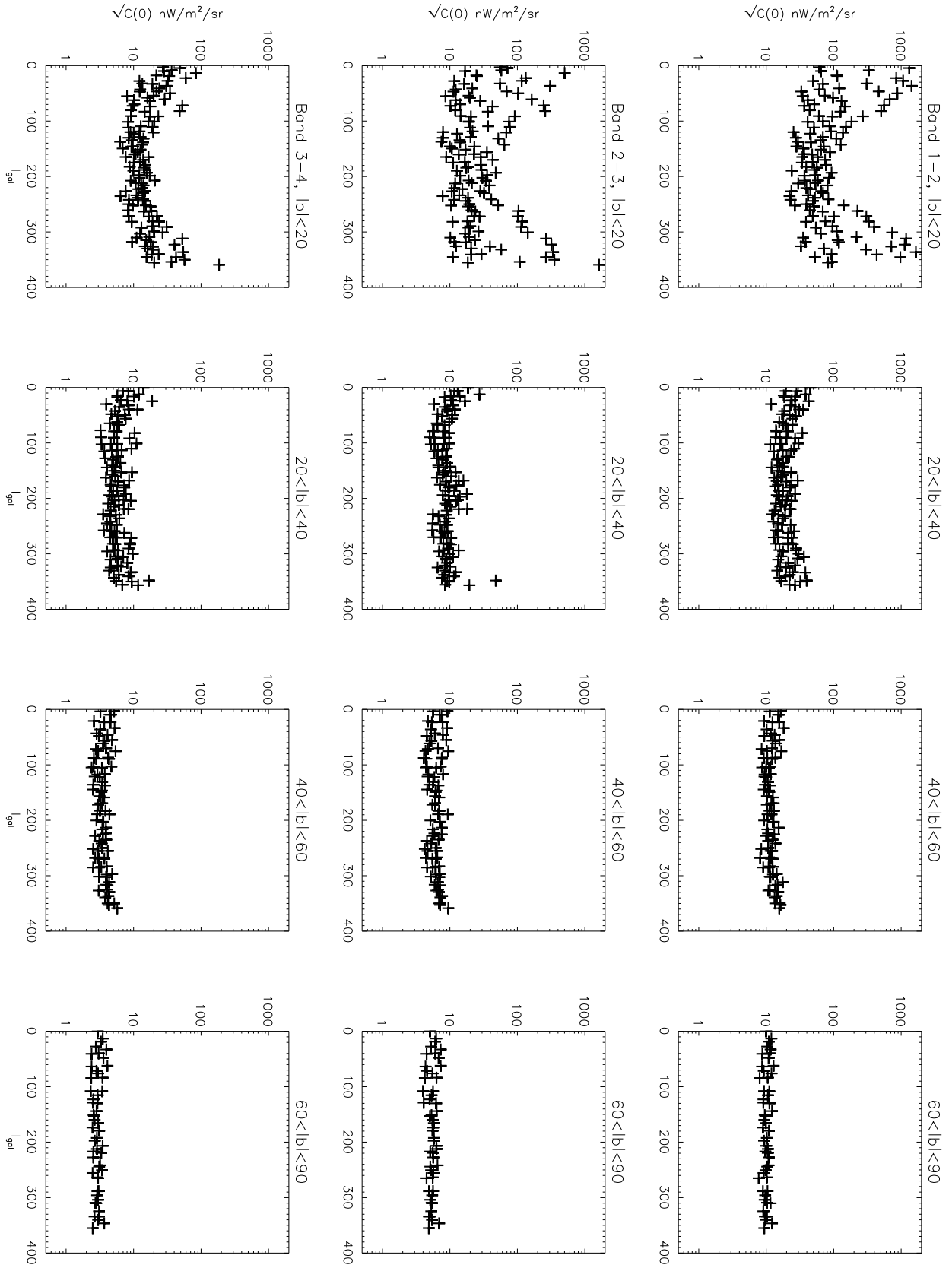


Fig. 9. —

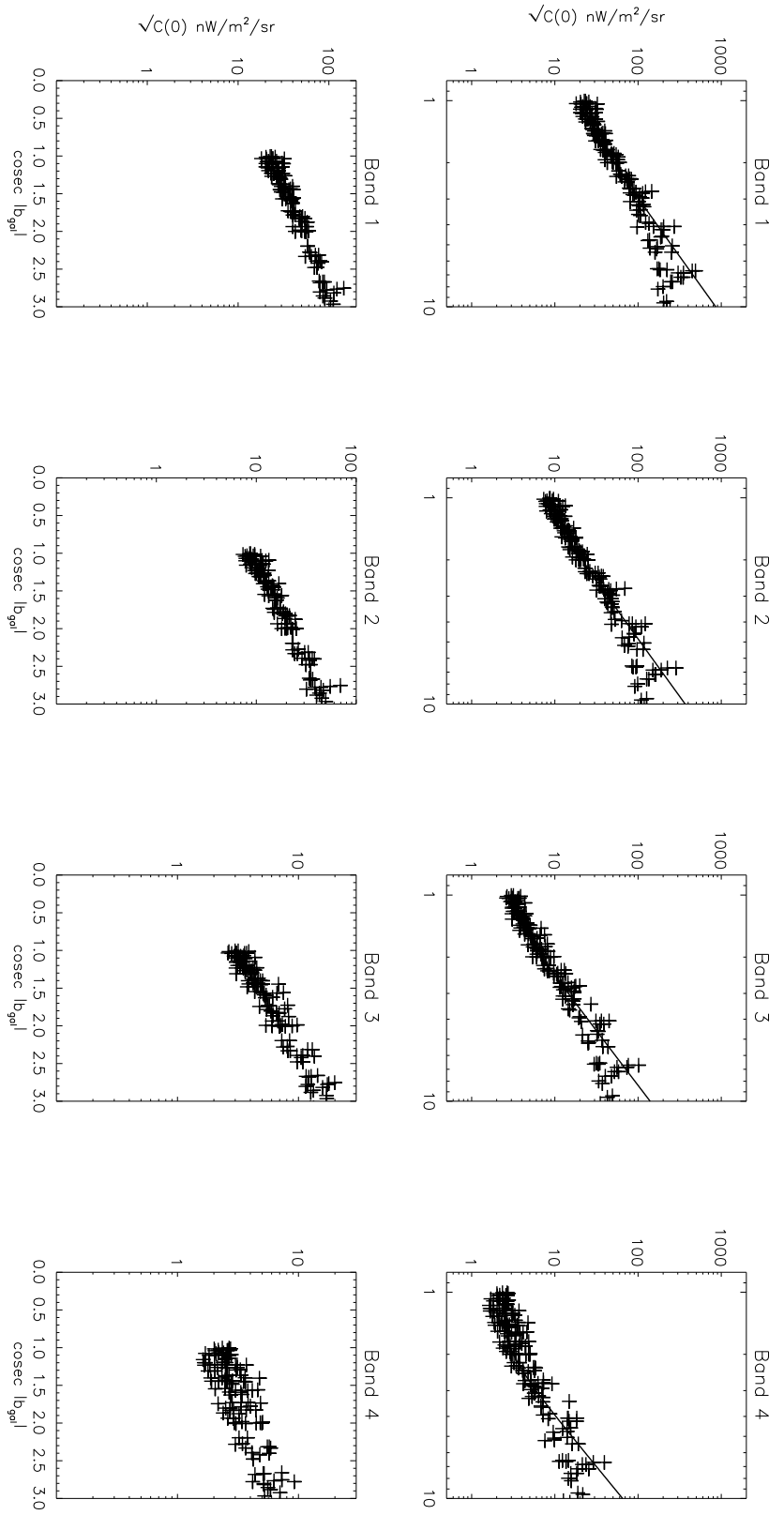


Fig. 10.—

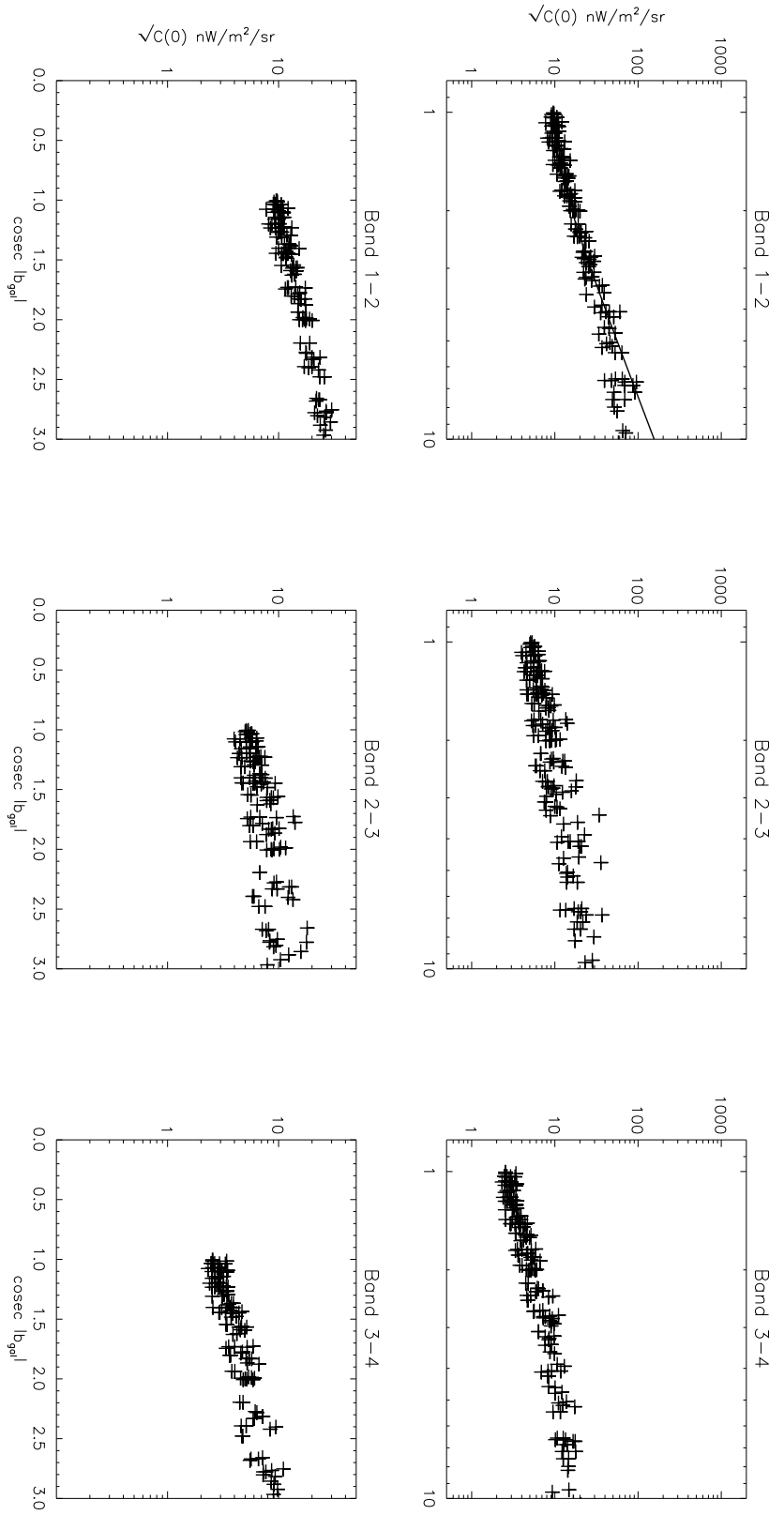


Fig. 11.—

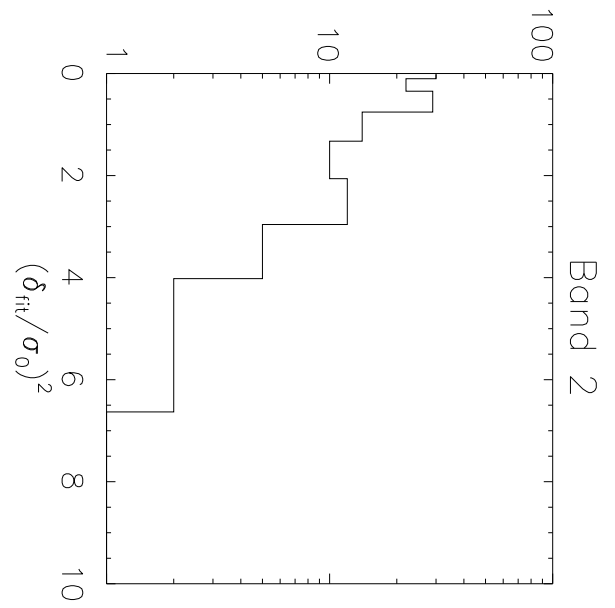


Fig. 12.—

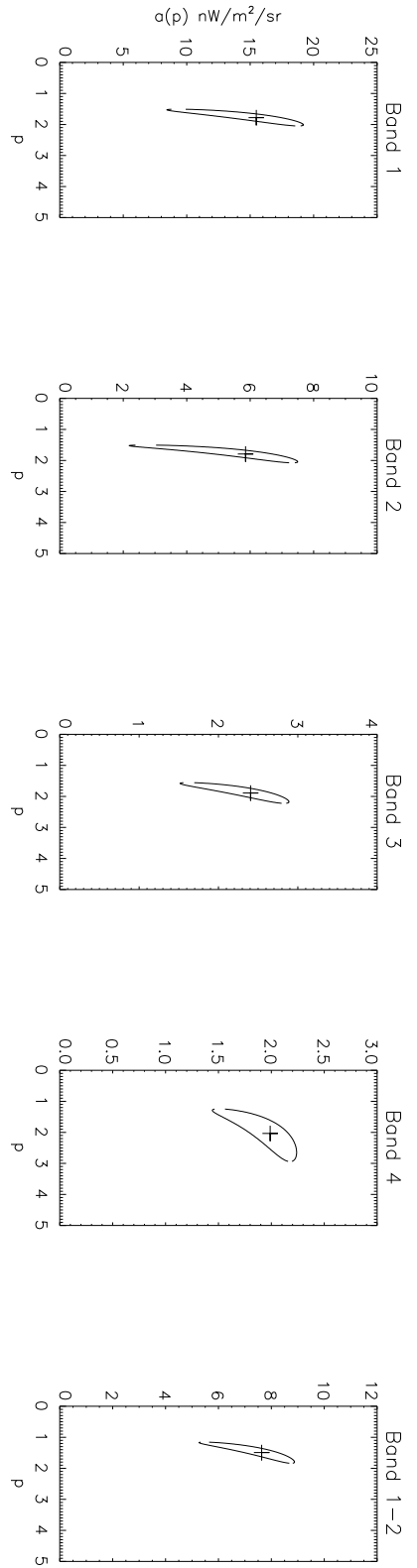


Fig. 13.—

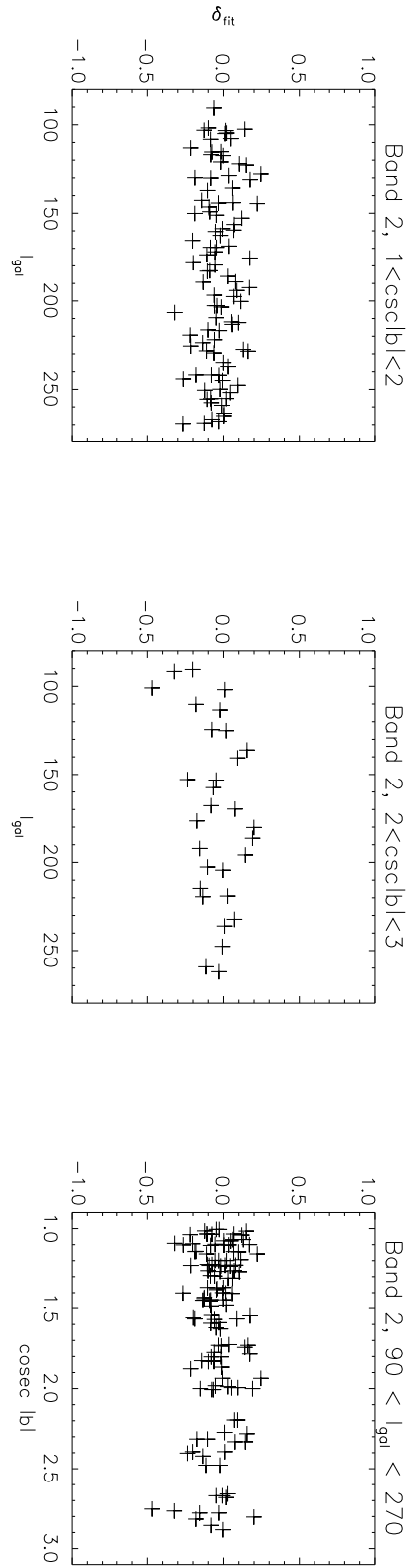


Fig. 14.—

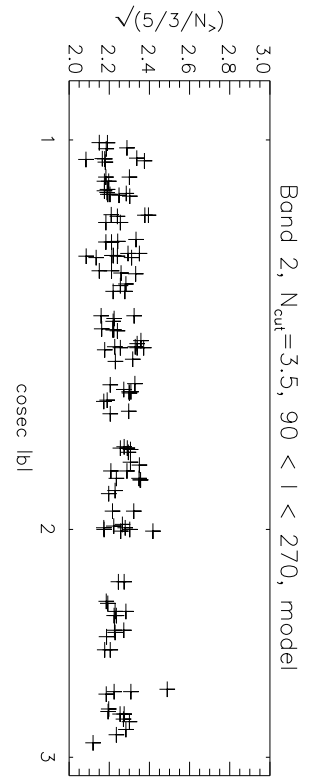
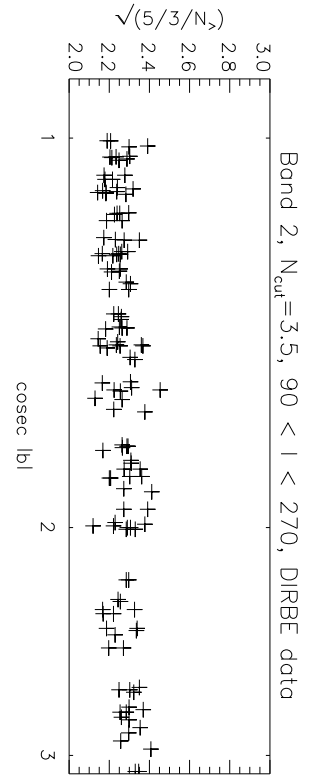


Fig. 15.—

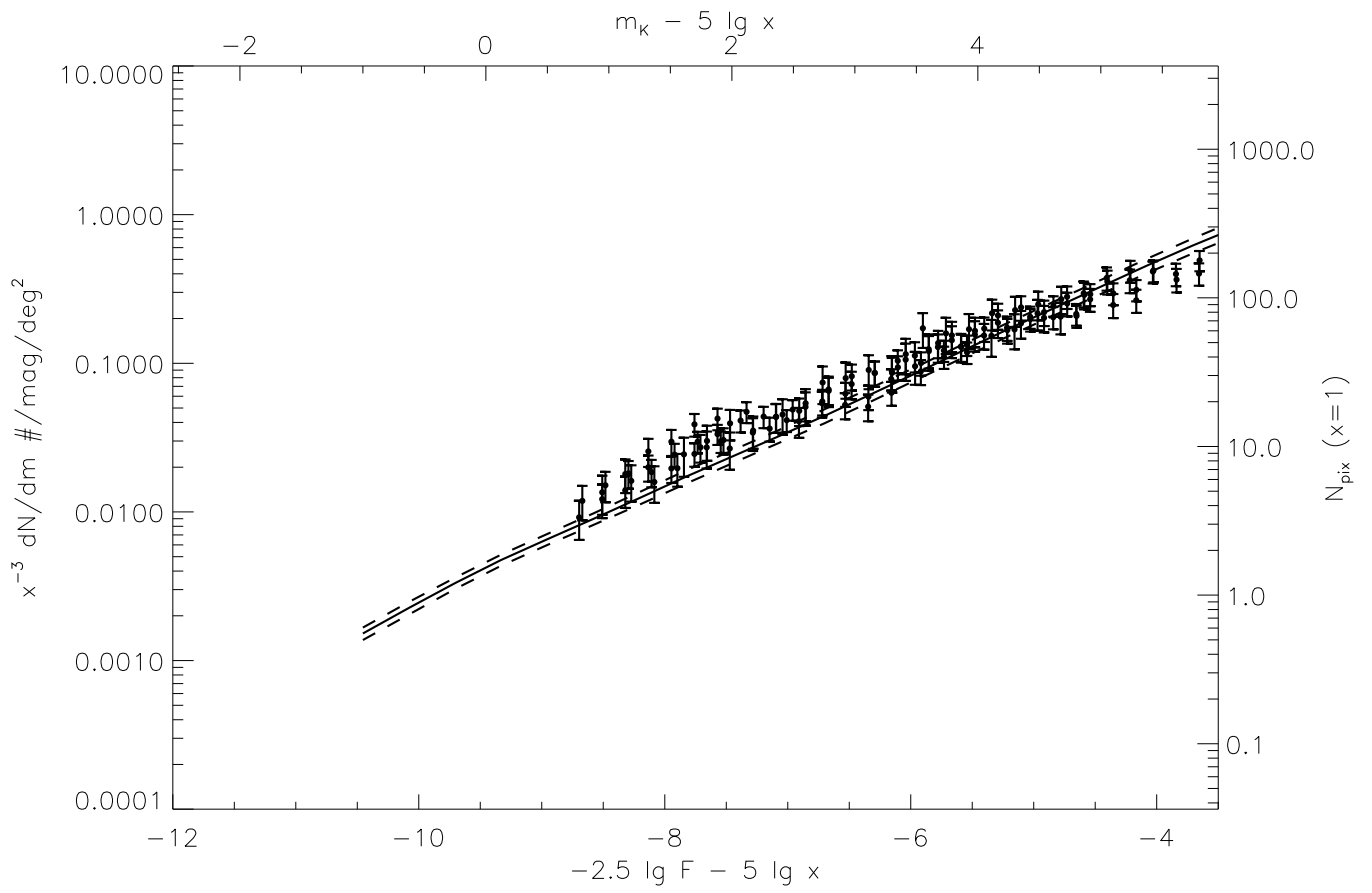


Fig. 16.—

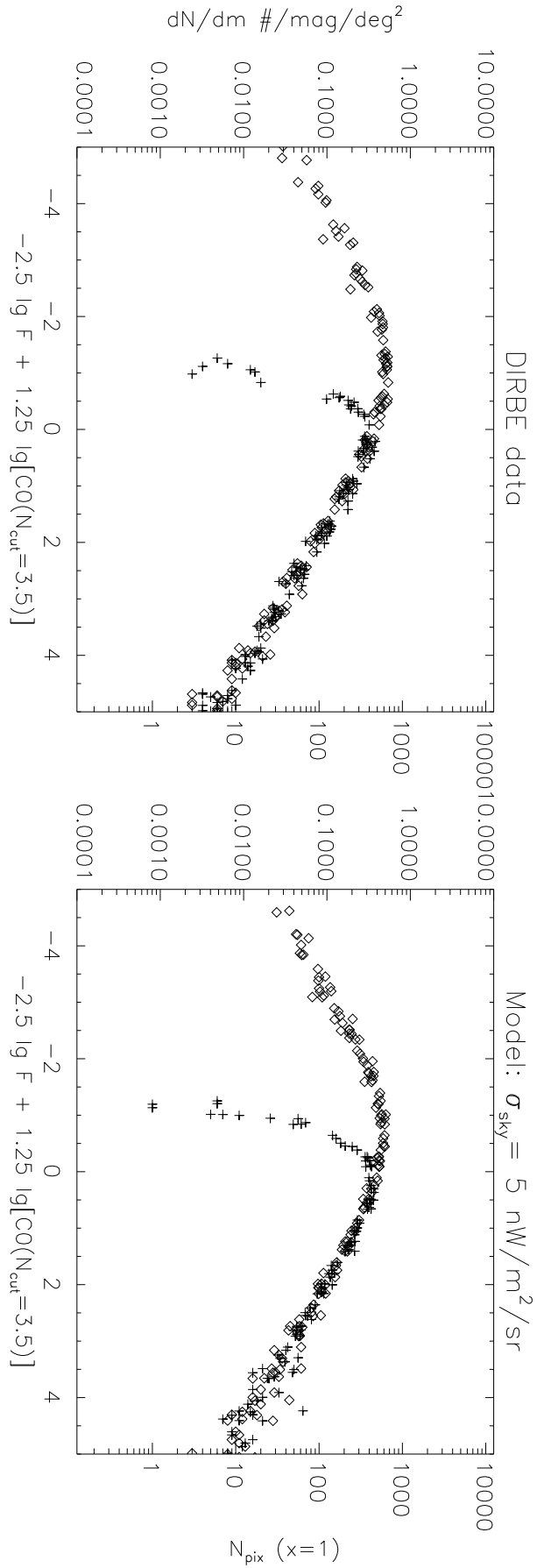


Fig. 17.—

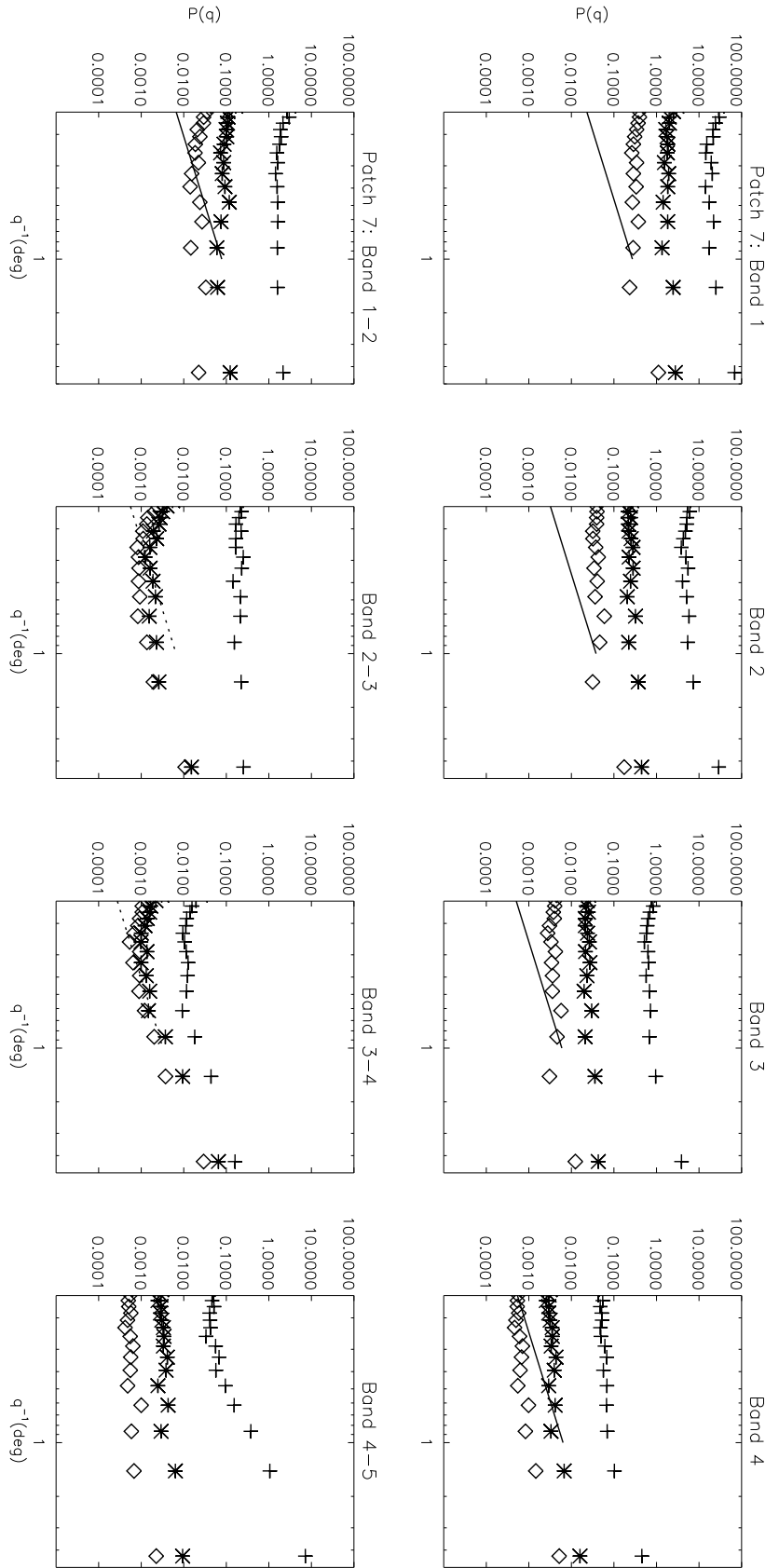


Fig. 18.—

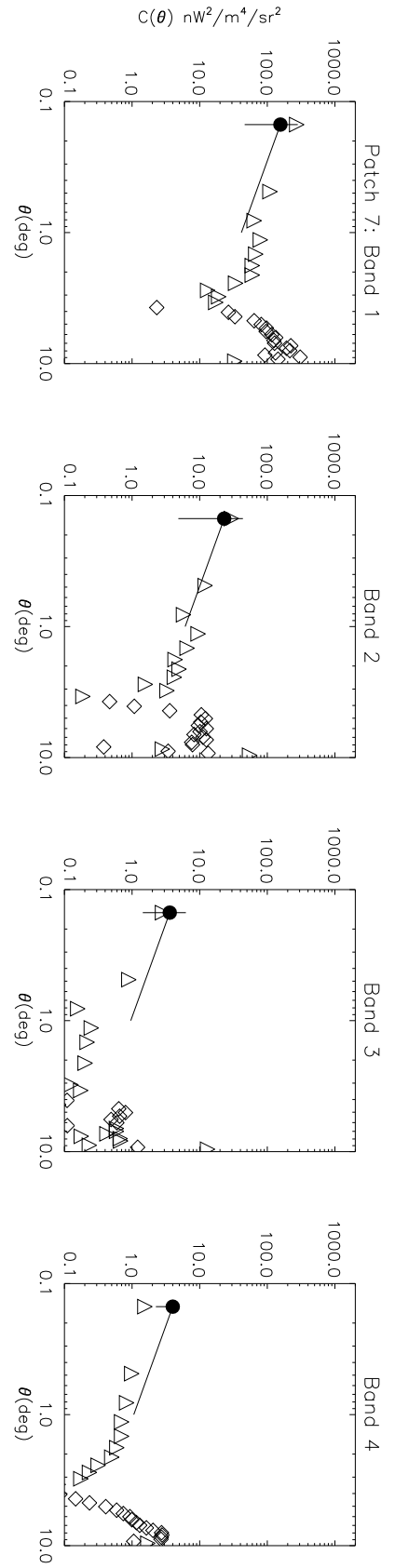


Fig. 19.—

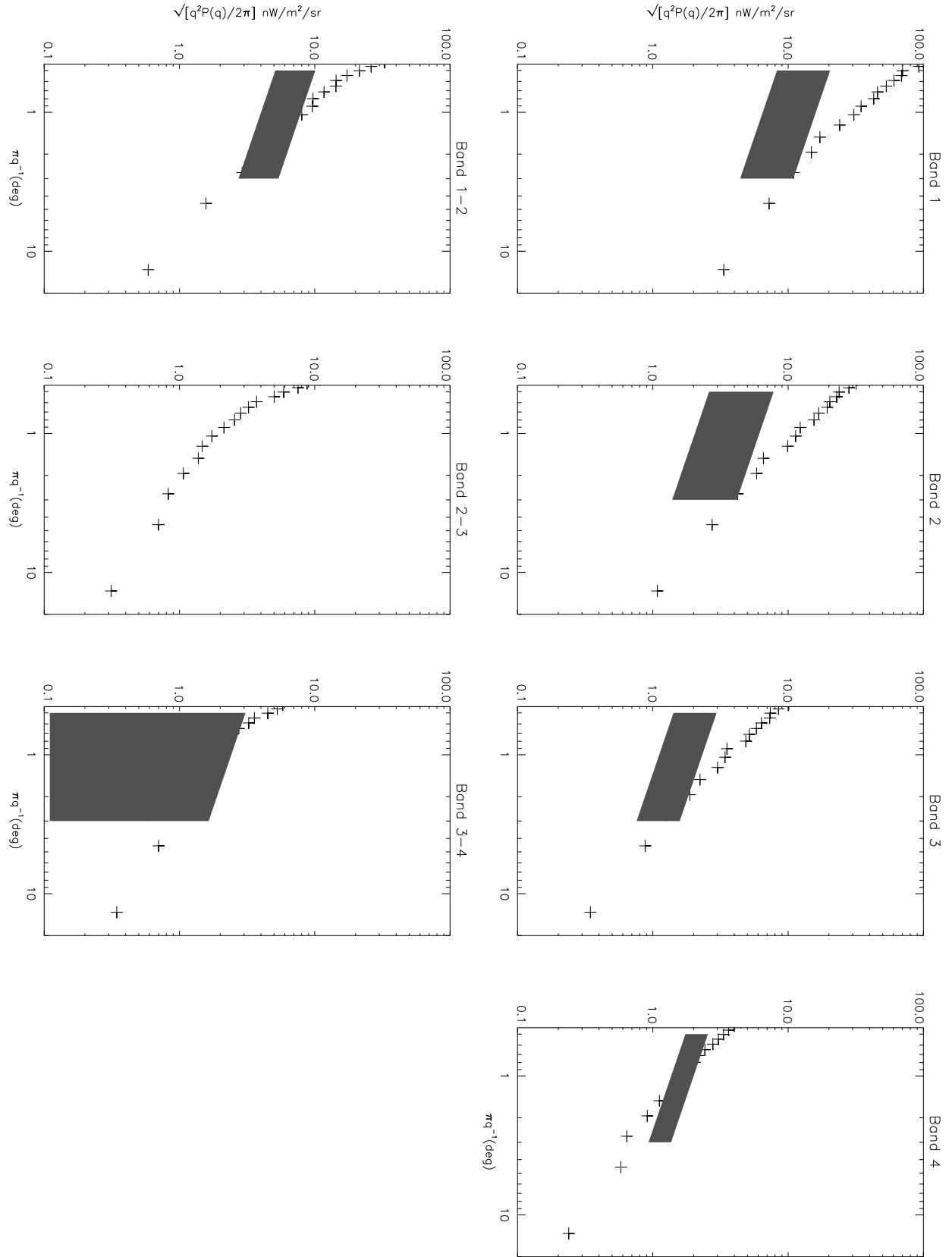


Fig. 20.—

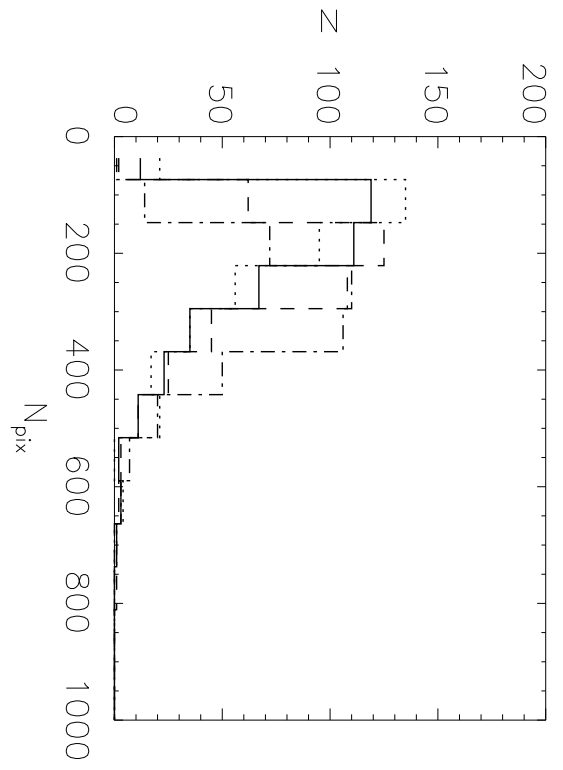


Fig. 21.—

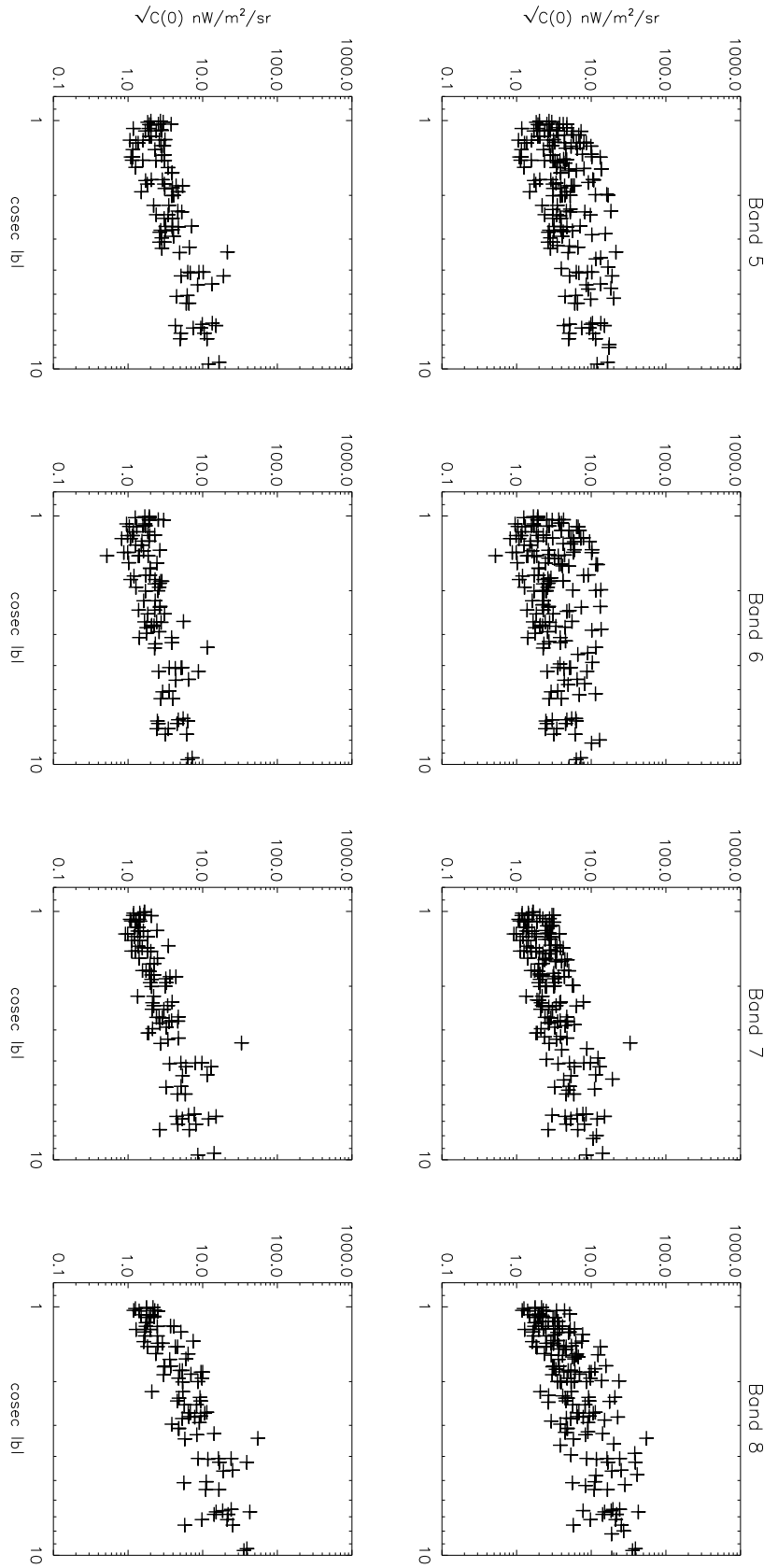


Fig. 22.—

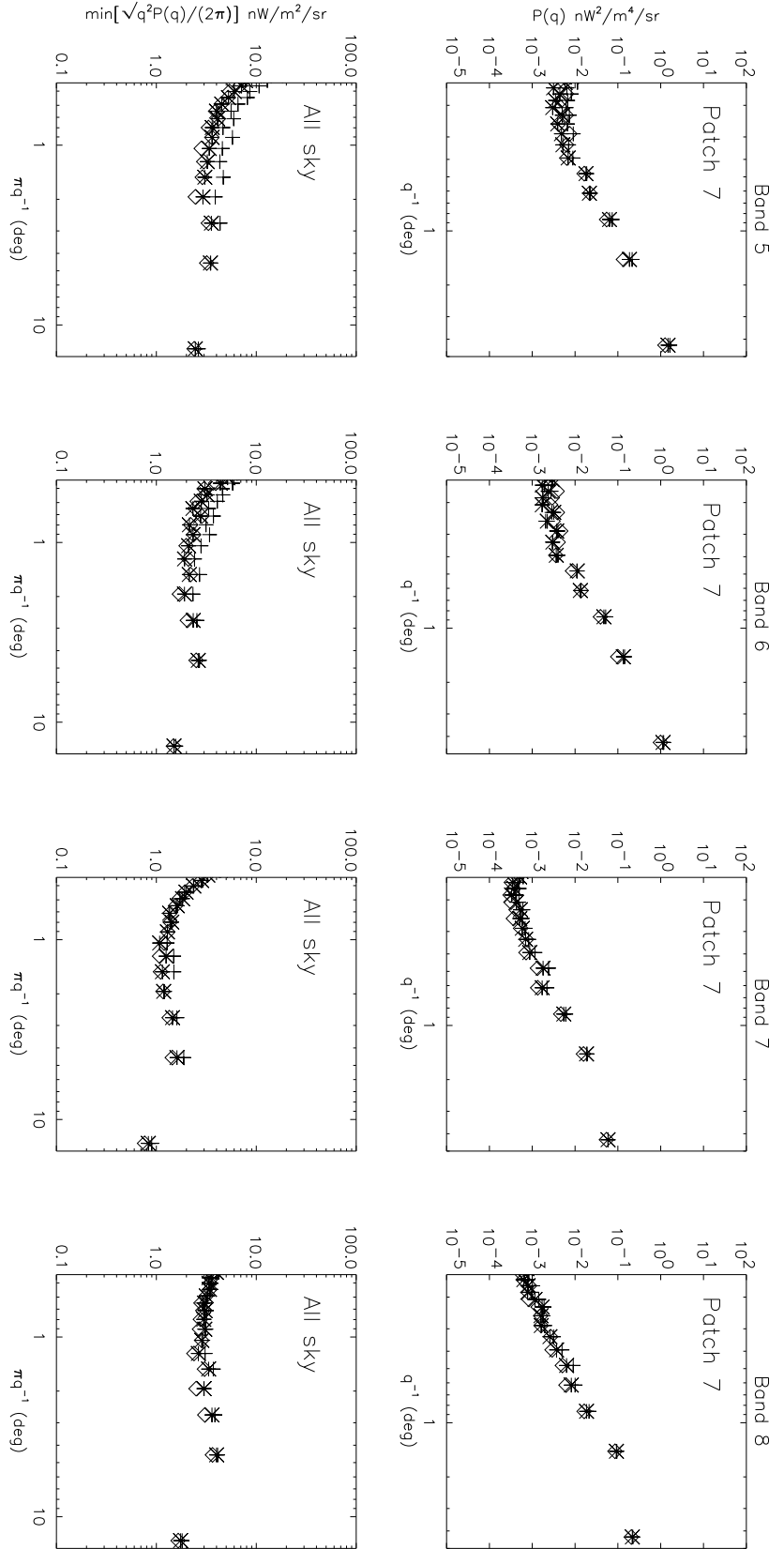


Fig. 23.—

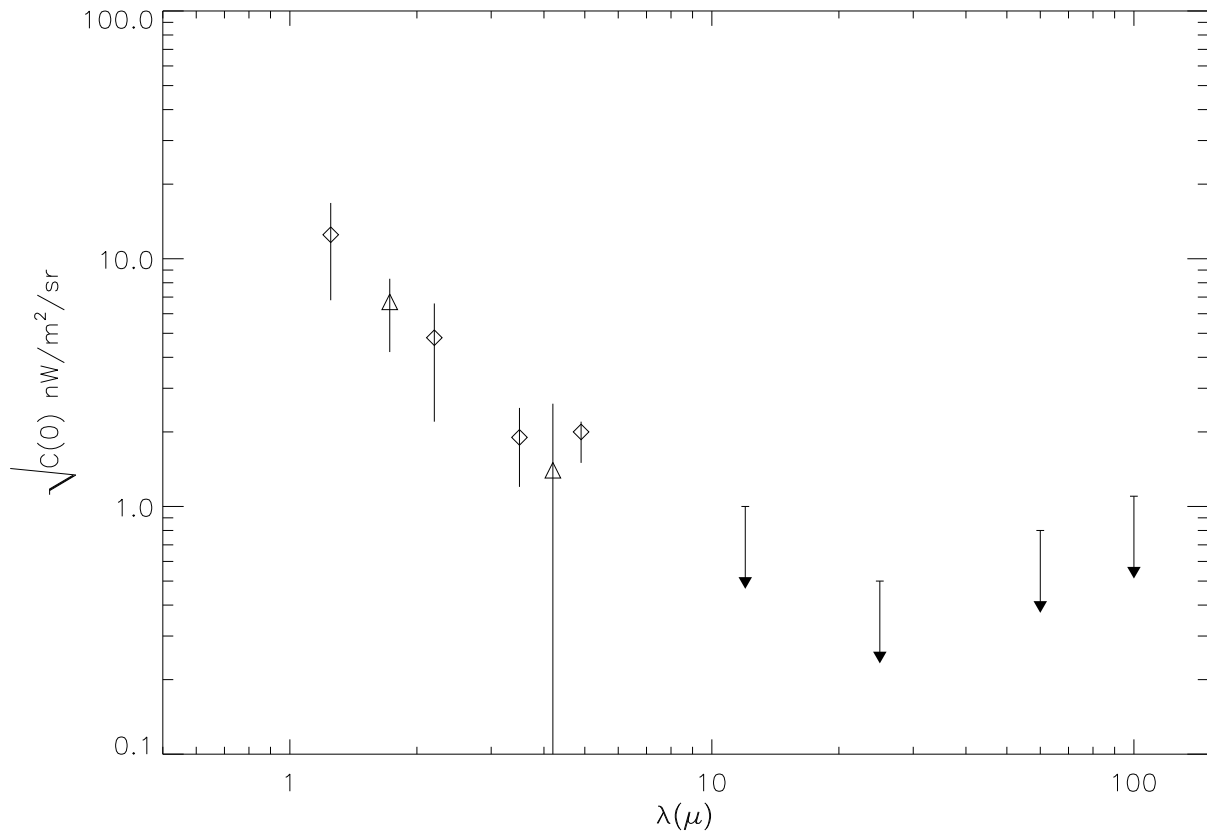


Fig. 24.—